Aerosol optical properties and direct radiative forcing based on measurements from the China Aerosol Remote Sensing Network (CARSNET) in eastern China

Huizheng Che[1*], Bing Qi[2], Hujia Zhao[1], Xiangao Xia[3,4], Thomas F. Eck[5], Philippe Goloub[6], Oleg Dubovik [6], Victor Estelles[7] , Emilio Cuevas-Agulló[8], Luc Blarel[6], Yunfei Wu[9], Jun Zhu[10], Rongguang Du[2], Yaqiang WANG[1], Hong Wang[1], Ke Gui[1], Jie Yu[1], Yu Zheng[10], Tianze Sun[1], Quanliang Chen[11], Guangyu Shi[12], Xiaoye Zhang[1*]

1 State Key Laboratory of Severe Weather (LASW) and Institute of Atmospheric Composition, Chinese Academy of Meteorological Sciences, CMA, Beijing, 100081, China

2 Hangzhou Meteorological Bureau, Hangzhou, 310051, China

3 Laboratory for Middle Atmosphere and Global Environment Observation (LAGEO), Institute of Atmospheric Physics, Chinese Academy of Sciences, Beijing, 100029, China

4 School of Geoscience University of Chinese Academy of Science, Beijing, 100049, China

5 Biospheric Sciences Branch, Code 923, NASA/Goddard Space Flight Center, Greenbelt, MD, USA.

6 Laboratoire d'Optique Amosphérique, Université des Sciences et Technologies de Lille, 59655, Villeneuve d'Ascq, France

7 Dept. Fisica de la Terra i Termodinamica, Universitat de Valencia, C/ Dr. Moliner 50, 46100 Burjassot, Spain

8 Centro de Investigación Atmosférica de Izaña, AEMET, 38001 Santa Cruz de Tenerife , Spain

9 Key Laboratory of Regional Climate-Environment for Temperate East Asia, Institute of Atmospheric Physics, Chinese Academy of Sciences, Beijing 100029, China

10 Collaborative Innovation Center on Forecast and Evaluation of Meteorological Disasters, Nanjing University of Information Science & Technology, Nanjing 210044, China

11 Plateau Atmospheric and Environment Key Laboratory of Sichuan Province, College of Atmospheric Sciences, Chengdu University of Information Technology, Chengdu, 610225, China

12 State Key Laboratory of Numerical Modeling for Atmospheric Sciences and Geophysical Fluid Dynamics (LASG), Institute of Atmospheric Physics, Chinese Academy of Sciences, Beijing, 100029, China

Corresponding author: chehz@cma.gov.cn & xiaoye@cma.gov.cn

Abstract

Aerosol pollution in eastern China is an unfortunate consequence of the region's rapid economic and industrial growth. Here, sunphotometer measurements from seven sites in the Yangtze River Delta (YRD) from 2011 to 2015 were used to characterize the climatology of aerosol microphysical and optical properties, calculate direct aerosol radiative forcing (DARF), and classify the aerosols based on size and absorption. Bimodal size distributions were found throughout the year, but larger volumes and effective radii of fine-mode particles occurred in June and September due to hygroscopic growth and/or cloud processing. Increases in the fine-mode in June and September caused AOD_{440nm} > 1.00 at most sites, and annual mean AOD_{440nm} values of 0.71-0.76 were found at the urban sites and 0.68 at the rural site. Unlike north China, the $AOD_{440\ nm}$ was lower in July and August (~0.40–0.60) than in January and February (0.71–0.89) due to particle dispersion associated with subtropical anticyclones in summer. Low volumes and large bandwidths of both fine- and coarse-mode aerosol size distributions occurred in July and August because of biomass burning. Single scattering albedos at 440 nm ($SSA_{440\ nm}$) from 0.91 to 0.94, indicated particles with relatively strong to moderate absorption. Strongly absorbing particles from biomass burning with a significant SSA wavelength dependence were found in July and August at most sites while coarse particles in March to May were mineral dust. Absorbing aerosols were distributed more-or-less homogeneously throughout the region with absorption aerosol optical depths at 440 nm ~0.04-0.06, but inter-site differences in the absorption Angström exponent indicate a degree of spatial heterogeneity in particle composition. The annual mean DARF was −93 ± 44 to −79 ± 39 W/m^2 at the Earth's surface and ~ −40 W/m^2 at the top of the atmosphere (for the solar zenith angle range of 50 to 80 degrees) under cloud free conditions. The fine-mode composed a major contribution of the absorbing particles in the classification scheme based on SSA, fine mode fraction, and extinction Angström exponent. This study contributes to our understanding of aerosols and regional climate/air quality, and the results will be useful for validating satellite retrievals and for improving climate models and remote sensing algorithms.

1. Introduction

Aerosols can have important effects on the Earth's climate over regional to global scales, but there are still uncertainties in the strengths and significance of these impacts (Hansen et al.2000; Solomon et al., 2007; Schwartz and Andreae, 1996). Aerosols affect the radiative balance of the Earth–atmosphere system by directly scattering and absorbing solar radiation (Charlson et al., 1992; Ackerman and Toon, 1981), and they can affect climate indirectly through aerosol–cloud interactions (Twomey et al., 1984; Albrecht et al., 1989; Li et al., 2016).

The physical and optical properties of aerosol particles determine their radiative effects, and information on these properties can be used to predict and assess global and regional changes in the Earth's climate (Eck et al., 2005; Myhre et al., 2009; IPCC, 2013; Panicker et al., 2013). Long-term, ground-based observations have contributed greatly to our understanding of the spatial variations in aerosols and their effects on the Earth's climate (Holben et al., 2001; Kaufman et al., 2002; Sanap and Pandithurai, 2014; Li et al., 2016). Ground-based monitoring networks have been established worldwide—for instance, AERONET (Aerosol Robotic Network) (Holben et al.,1998; Goloub et al., 2007), SKYNET (SKYrad Network) (Takamura et al., 2004), EARLINET (European aerosol Lidar network) (Pappalardo et al., 2014) and the GAW-PFR Network (Global Atmosphere Watch Programmer-Precision Filter Radiometers) (Wehrli, 2002; Estelles et al., 2012). In China, CARSNET (the China Aerosol Remote Sensing NETwork) and CSHNET (the Chinese Sun Hazemeter Network) were established to obtain data on aerosol optical characteristics (Che et al., 2009a, 2015b; Xin et al., 2007). High-frequency, ground-based measurements of aerosol optical properties made at these stations have improved our understanding of the sources, transport, and diurnal variations of air pollutants, and they have provide insights into the aerosols' effects on climate. Ground-based observations are also useful for the validation of satellite retrievals (Holben et al., 2017; Xie et al., 2011).

Most of the ground-based studies of the optical properties of aerosols in China have been conducted in urban regions that have been undergoing rapid economic development. Those sites typically have had high aerosol loadings and in many cases serious environmental

problems (Cheng et al., 2015; Pan et al., 2010; Xia et al., 2013; Wang et al., 2015; Che et al., 2015a). Detailed information on aerosol optical depth (AOD), the types of aerosols, and especially the size and absorption properties of ambient populations over a wide sampling of regions is needed to understand the effects of aerosols on the Earth's climate and the environment (Giles et al., 2011; Che et al., 2009b; Wang et al., 2010; Zhu et al., 2014). In particular, the aerosol direct radiative forcing is sensitive to the aerosol radiation absorptivity (Haywood and Shine, 1995). Therefore, it is important to understand the connections between the aerosol types and absorption properties because that information can be used for comparisons and validation of chemical transport models and satellites (Lee et al., 2010).

The Yangtze River Delta (YRD) region in eastern China has recently undergone rapid economic growth, and the loadings of aerosols in the region can be very high during heavy pollution episodes (Fu et al., 2008; Zhang et al., 2009). Studies of aerosol optical properties in eastern China have contributed to our understanding of local air quality and regional climate impacts (Duan and Mao, 2007; Pan et al., 2010; Ding et al., 2016). In the YRD, investigations of aerosol optical properties have been conducted in Nanjing, Hefei, Shanghai, Shouxian and Taihu (Zhuang et al. 2014; Li et al., 2015; Wang et al., 2015; He et al., 2012; Lee et al., 2010; Cheng et al., 2015; Xia et al., 2007). Those studies mostly involved sampling at single sites ~100 km apart from one other without synchronous observations, and many have been of relatively short duration, and so there remains a need for more extensive ground-based measurements.

For the present study, sampling was conducted over a period of several years to better characterize the climatology of the aerosol microphysical and optical properties, including aerosol absorptivity, and to improve estimates of direct aerosol radiative forcing. For these studies, sun photometer measurements were made at 3 min intervals from 2011 to 2015 at seven CARSNET sites (one densely populated urban site, five urban center sites in smaller cities, and one rural site) ~10–40 km apart in the YRD. The dense network of ground-based sun- and sky-scanning spectral radiometers improves the temporal and spatial coverage of the data, and that has enabled us to capture small-scale variations in the aerosols. The results not

120 only contribute to our understanding of regional climate and local air quality impacts, but they
121 also will be useful for validation of satellite data and improving the performance of models and
122 remote sensing algorithms in the future.

123 This paper is organized as follows: Section 2 describes the sites, the methods used for
124 retrieving the aerosol optical properties and their uncertainties, and the calculation of aerosol
125 direct radiative forcing from the retrieved aerosol optical parameters. Section 3 presents the
126 aerosol microphysical properties, optical properties, and calculations of direct radiative forcing.
127 The aerosol type classification is also presented based on the aerosol optical parameters.
128 Then a brief discussion is made about the analysis of this study. Section 4 is the conclusions.

129 **2. Site descriptions, measurements and methods**

130 Figure 1 shows the locations of the seven CARSNET sites of the YRD, and detailed
131 information on the sites is included in Table 1. Hangzhou is a densely populated urban site with
132 a heavy vehicular traffic, and it is affected by various types of anthropogenic emissions. LinAn,
133 Fuyang, Jiande, Xiaoshan and Tonglu are urban center sites in smaller cities, and they are all
134 affected to varying degrees by anthropogenic activities, especially pollutants from industries
135 and agriculture. The rural site of ChunAn has a small population, and there are few industrial
136 sources nearby so the effects from local or regional pollution are relatively small.

137 Sun photometers (CE-318, Cimel Electronique, Paris, France) were installed at each of
138 the seven sites and operated from 2011 to 2015. These instruments were standardized and
139 calibrated using CARSNET reference instruments (Che et al., 2009a), which in turn were
140 periodically calibrated at Izaña, Tenerife, Spain in conjunction with the AERONET program.
141 The cloud-screened AODs (based on the work of Smirnov et al. 2000) at 340, 380, 440, 500,
142 670, 870, 1020 and 1640 nm with uncertainties less than 0.01 (Eck et al., 1999) were obtained
143 using ASTPwin software (Cimel Electronique). The water vapor expressed as precipitable
144 water in the column was derived from the 940 nm channel with uncertainties less than 10%
145 (Eck et al., 1999). Daily averages and statistical analysis were calculated for days on which
146 instantaneous AOD measurements were made more than ten times (Che et al., 2015b). The

147 extinction Angström exponent values (EAE) were calculated from AOD values at 440 and 870
148 nm.

149 Aerosol microphysical properties were retrieved from the almucantar sky irradiance
150 measurements in conjunction with measured spectral AOD, following the methods of Dubovik
151 and King (2000) and Dubovik et al. (2002, 2006). The dataset contained information on (1)
152 volume size distributions in 22 size bins for particle radii 0.05–15 μm; (2) fine and coarse mode
153 aerosol effective radii; and (3) aerosol optical properties—including the wavelength dependent
154 single-scattering albedo (SSA), the complex refractive index, the absorption AOD (AAOD), and
155 the absorption Angström exponent (AAE). For the retrieval process, the surface albedo (SA)
156 was interpolated/extrapolated to 440, 670, 870, and 1020 nm from the daily Moderate
157 Resolution Imaging Spectroradiometer (MODIS) surface reflectance product of MCD43C3
158 (https://ladsweb.modaps.eosdis.nasa.gov/). Following the procedures of Dubovik et al.
159 (2002, 2006), all particles smaller than 0.992 μm were considered fine mode particles while
160 those larger than 0.992 μm were considered coarse mode. And the effective radii for the total
161 ($Reff_t$), fine ($Reff_{fine}$) and coarse ($Reff_{coarse}$) mode aerosols are calculated as follows:

162 $$R_{eff} = \frac{\int_{r_{min}}^{r_{max}} r^3 \frac{dN(r)}{dlnr} dlnr}{\int_{r_{min}}^{r_{max}} r^2 \frac{dN(r)}{dlnr} dlnr} \quad (1)$$

163 Where r_{min} is 0.05, 0.05, and 0.992 μm and r_{max} is 15, 0.992, and 15 μm for the total, fine
164 and coarse mode aerosols, respectively.

165 The inversion algorithm used for calculating the aerosol volume distribution ($dV/\ln r$)
166 assumed a homogeneous distribution of non-spherical aerosol particles as in the work of
167 Dubovik (2006); this approach has been widely applied in studies of many different areas of
168 the world. The SSA was retrieved using only AOD_{440nm} > 0.40 measurements to avoid the
169 large uncertainties inherent in low AOD retrievals (Dubovik et al. 2002, 2006). Real and
170 imaginary parts of refractive index at 440, 675, 870, and 1020 nm were constrained to the
171 ranges of 1.33–1.60 and 0.0005–0.50, respectively (Dubovik and King, 2000; Che et al.,
172 2015b). The complex refractive index is assumed independent of particle size. This

assumption is valid for fine or coarse-dominated cases, however, could cause some errors in SSA and particle size retrievals for mixed aerosol scenarios (Xu and Wang, 2015; Xu et al 2015). The AOD, AAOD, and AAE are related to one another as shown in equations (2) and (3):

$$AAOD(\lambda) = [1 - SSA(\lambda)] \times AOD(\lambda) \quad (2)$$

$$AAE = -d\ln[AAOD(\lambda)]/d\ln(\lambda) \quad (3)$$

The inversion algorithms mentioned above have been used for AERONET and CARSNET, and the accuracies of the volume size distribution were 15-25% for 0.1 μm ≤ r ≤ 7.0 μm and 25-100% for r < 0.1 μm and r >7μm. The accuracies for both AOD and AAOD are ~0.01. The errors for the total, fine and coarse mode SSA are about 0.030, 0.037 and 0.085, respectively. The imaginary and real parts of the complex refractive index for the AOD at 440 nm > 0.40 and a solar zenith angle > 50° have errors of ~0.0025–0.0042 and 0.04, respectively (Dubovik et al., 2000; Li et al., 2015a).

The direct aerosol radiative forcing (DARF) values in units of W/m^2 were calculated using the radiative transfer module in the AERONET inversion (García et al., 2008; 2012) under the assumption of cloud-free conditions. The DARF is defined as the difference in the shortwave radiative fluxes between the two energy levels including and excluding aerosol effects at the Earth's surface (bottom of the atmosphere, BOA) and the top of the atmosphere (TOA) in equations (4) and (5) as follows:

$$\mathrm{DARF}_{TOA} = F_{TOA}^{\uparrow 0} - F_{TOA}^{\uparrow} \quad (4)$$

$$\mathrm{DARF}_{BOA} = F_{BOA}^{\downarrow} - F_{BOA}^{\downarrow 0} \quad (5)$$

where F and F^0 represent the broadband fluxes with and without aerosols at BOA and TOA, respectively. The arrows in these equations indicate the direction of the fluxes for the downward and upward cases. Defined this way, a negative value for DARF indicates aerosol cooling effects while positive values imply warming, both at the BOA and the TOA.

198 In the radiative transfer module used here, the flux calculations accounted for absorption
199 and multiple scattering effects using the Discrete Ordinates (DISORT) approach (Stamnes et
200 al., 1988; Nakajima and Tanaka, 1988). The solar broadband fluxes from 0.2 to 4.0 μm were
201 simulated by using information on aerosol properties (size distribution, spectral AOD, SSA,
202 and phase function) obtained from the ground-based measurements. The spectral refractive
203 indices (both real and imaginary parts) were interpolated/extrapolated from the values
204 retrieved at four distinct wavelengths (440, 670, 870, 1020 nm) from the ground-based sun
205 photometers. Likewise, the spectral dependence of surface reflectance was
206 interpolated/extrapolated from surface albedo values used in the aerosol property retrieval
207 process for the same wavelengths.

208 The integrated effects of atmospheric aerosol scattering and absorption, gaseous
209 absorption, and molecular scattering and underlying surface reflection effects were evaluated
210 using the Global Atmospheric ModEl (GAME) code (Dubuisson et al., 1996; Roger et al., 2006).
211 In the GAME code, gaseous absorption (mainly H_2O, CO_2, and O_3), is calculated from the
212 correlated k-distribution (Lacis and Oinas, 1991). The instantaneous column water vapor
213 content was retrieved by the absorption differential method from the 0.94 mm channel
214 (Smirnov et al., 2004). The total ozone content was taken from monthly climatology values
215 based on the Total Ozone Mapping Spectrometer (TOMS) measurements. The GAME model
216 accounts for spectral gaseous absorption; that is, ozone in the ultraviolet-visible spectral range
217 (0.20–0.35 μm and 0.5–0.7 μm) and water vapor in the shortwave infrared spectrum (0.8–3.0
218 μm).

219 The flux calculations were performed for a multi-layered atmosphere with the US standard
220 1976 atmosphere model for gaseous distributions and single fixed aerosol vertical distribution
221 (exponential with an aerosol height of 1 km) (Gacia et al., 2008). As these authors have
222 pointed out, solar fluxes calculated using the module described above show excellent
223 agreement with ground-based measurements of solar radiation (slope of 0.98 ± 0.00 and bias
224 of -5.32 ± 1.00 W/m^2) with a correlation of 99%. There is a small overestimation of +9 ± 12
225 Wm^{-2} of the observed solar radiation at the surface in global terms, and this corresponds to a

relative error of +2.1 ± 3.0%. The differences range from +14 ± 10 Wm^{-2} to +6 ± 13 Wm^{-2} for urban-industrial and biomass burning aerosols, respectively. The errors are expected to be of the same magnitude at the TOA, since the same methodology and inputs are used at both levels (gaseous and aerosol distribution, radiative model, etc).

3. Results and discussion

3.1 Aerosol microphysical properties: particle radius and volume size distributions

Figure 2 shows the monthly aerosol size distribution (d*V*/dln*r*) for all seven sites in the YRD. The annual mean values for the effective radii of the total particles (R_{efft}) were ~0.30 μm, and the average annual volume was ~0.18 $\mu m^3/\mu m^2$ (Table 1). The fine-mode effective radii averaged ~0.16 μm in the YRD with a fractional volume of 0.10–0.11 $\mu m^3/\mu m^2$ while the coarse-mode average effective radii were ~2.2 μm with a fractional volume ~0.08 $\mu m^3/\mu m^2$. These results show that there was a larger contribution of fine-mode particles to the aerosol volume compared with the coarse mode at all sites. The total and fine-mode aerosol volumes and effective radii showed small differences from the densely populated urban site (Hangzhou), to the urban center sites in smaller cities (Xiaoshan, Fuyang, LinAn, Tonglu, Jiande) or the rural site (ChunAn), and this reflects a generally homogeneous distribution of the aerosol in the YRD. The coarse-mode aerosol volumes also showed small differences among site, but the range of effective radii varied 2.16–2.30 μm.

Higher volumes and larger effective radii of the fine-mode were observed in June and September at most sites, and again there were relatively small differences among sites; the exception was Xiaoshan where the month-to-month differences in these variables were less pronounced (Fig. 2). The increases in submicron particles during the summer may have been caused in part by the hygroscopicity of the aerosols. In this regard, Saha et al. (2004) reported the volume of accumulation mode particles increased faster than the coarse-mode under high relative humidity conditions. At our sites, the precipitation in June and September was greater than in the other months because of the “Meiyu flood period” and the “typhoon and autumn rain period”, respectively. Indeed, the major aerosol components, which include sulfate, nitrate,

ammonium, and organic compounds, can cause severe haze-fog events during high relative humidity conditions. Fine particles containing sulfate, nitrate, and ammonium are hygroscopic, and their sizes are strongly affected by the relative humidity (Fu et al., 2008; Shen et al., 2015; Li et al., 2015b; Huang et al., 2016). Additionally, broad fine-mode distributions may result from the occurrence of fog or low-altitude cloud dissipation events (Eck et al. 2012; Li et al., 2010, 2014). Eck et al. (2012) also pointed out that a large range of fine-mode aerosol sizes may result from cloud processing, and that also could contribute to a shoulder of larger size particles in the accumulation mode, especially in regions where sulfate and other water-soluble aerosols exist. Another interesting observation is that the fine-mode aerosol volume in July was relatively low at all sites, and is coincident with lower relative humidity in July (~60%) compared with that in June (~80%) in the YRD. Therefore, the hygroscopic effects on fine particles in July evidently are not as obvious as in June or September.

High volumes for coarse-mode aerosol occurred in March to May at all sites, and this suggests that more large particles occurred in spring than in the other seasons. The most likely explanation for this is the presence of mineral dust in the YRD region at that time of year. High PM_{10} mass concentrations of Hangzhou during 2012-2015 showed 78.5 ± 15.4, 84.7 ± 11.3, and 83.6 ± 15.5 μg/m^3 in March, April, and May, respectively (see the supplement), which is consistent to the results of relative large coarse-mode aerosol volumes in this study. As Cao et al. (2009) pointed out, fugitive dust can account for about one-third of PM_{10} mass concentration in Hangzhou, and that mainly came from re-suspended road dust and construction soil. The long-range transportation of dust in spring from northern/northwestern China could also contribute to the high coarse-mode aerosol volume. For instance, Fu et al. (2014) and Sun et al. (2017) found that dust particles could be transported long distances, and the impacts were apparent in the YRD. Low volumes and large bandwidths of coarse-mode aerosol were found in July and August at all sites, and that may have been due to the wet removal of coarse particles by the heavy precipitation in June. In July and August, strong convection associated with subtropical anticyclone can disperse the aerosol. These results also are consistent with previous reports showing minimum PM_{10} concentrations in summer of the YRD region (Cao et al., 2009). It was found the PM_{10} mass concentrations of Hangzhou

during 2012-2015 were relative low with values 53.2 ± 6.8, and 56.7 ± 4.4 μg/m^3 in July and August, respectively (see the supplement) Sun et al. (2013) found that aerosol size distributions can broaden under unstable weather conditions, and in July and August, the Weather in the YRD can become unstable due to the high temperatures, and this could be another factor that contributed to the large bandwidth of both fine- and coarse-mode particles in our study. However, these possible connections should be re-visited in the future.

3.2 Aerosol optical properties: AOD and EAE

The arithmetic mean annual values for AOD_{440nm} at the six urban sites (Hangzhou, Xiaoshan, Fuyang, LinAn, Tonglu, Jiande) were 0.71-0.76 and 0.68 at the rural site of ChunAn (Table 1). The difference in AOD between urban and rural sites was <10%, and this indicates there were widespread anthropogenic impacts on the aerosol populations in the YRD and that the high particle concentrations extend beyond the local to the regional scale. Nonetheless, the AOD_{440nm} generally decreased from the east coast to inland areas towards the west (0.76 at Hangzhou, 0.73 at LinAn, 0.71 at Jiande, and 0.68 at ChunAn), and this can be explained by stronger anthropogenic impacts in the more urbanized east. The high AOD_{440nm} at Hangzhou was likely the result of the greater industrial activity and higher population density in the eastern part of that metropolitan region; both of those factors could lead to larger aerosol emissions compared with the less populated urban and rural sites. The coarse-mode AOD values were just ~0.06 to 0.08, and ratios of the fine-mode $AOD_{440\ nm}$ to the total $AOD_{440\ nm}$ varies from 0.89-0.91 at the sites, and therefore, fine-mode particles clearly were the main contributors to light extinction in the region. The less coarse mode fraction of total aerosol extinction (~10%) indicated that the contribution of coarse particles to aerosol loading in the YRD region is not as obvious as in other north/northeast China region (Zhang et al., 2012).

305 Table1.Geographical location and annual arithmetic mean optical parameters for aerosols from seven sites in the Yangtze River Delta.

	Hangzhou	Xiaoshan	Fuyang	LinAn	Tonglu	Jiande	ChunAn
Site type	Urban	Suburban	Suburban	Suburban	Suburban	Suburban	Rural
Longitude (°E)	120.19	120.25	119.95	119.72	119.64	119.27	119.05
Latitude (°N)	30.26	30.16	30.07	30.23	29.80	29.49	29.61
Altitude (m)	41.9	14.0	17.0	139	46.1	88.9	171.4
[a]N_{day}	485	180	217	562	498	480	439
[b]$N_{inst.}$	2052	752	906	2410	2255	1952	1731
[c]AOD_{440nm}	0.76±0.42	0.76±0.43	0.76±0.45	0.73±0.44	0.71±0.41	0.73±0.40	0.68±0.38
[c]$AOD_{fine(440nm)}$	0.68±0.42	0.69±0.41	0.69±0.44	0.66±0.43	0.64±0.41	0.66±0.40	0.61±0.38
[c]$AOD_{coarse(440nm)}$	0.08±0.06	0.07±0.06	0.07±0.06	0.07±0.07	0.07±0.06	0.07±0.07	0.06±0.05
[d]$EAE_{440\text{-}870\ nm}$	1.29±0.26	1.37±0.24	1.32±0.24	1.29±0.27	1.30±0.26	1.32±0.28	1.22±0.25
[c]SSA_{440nm}	0.91±0.06	0.93±0.04	0.94±0.04	0.93±0.05	0.92±0.04	0.92±0.05	0.94±0.03
[e]SSA_{670nm}	0.92±0.06	0.91±0.06	0.93±0.06	0.92±0.05	0.93±0.05	0.92±0.07	0.94±0.03
[f]SSA_{870nm}	0.90±0.07	0.90±0.07	0.91±0.08	0.91±0.06	0.91±0.06	0.90±0.08	0.93±0.04
[g]SSA_{1020nm}	0.89±0.08	0.89±0.08	0.89±0.09	0.90±0.07	0.90±0.07	0.90±0.09	0.92±0.05
[c]$AAOD_{440\ nm}$	0.06±0.05	0.05±0.04	0.04±0.04	0.05±0.04	0.05±0.04	0.06±0.04	0.04±0.03
[d]$AAE_{440\text{-}870\ nm}$	1.13±0.46	0.88±0.42	0.85±0.43	0.98±0.35	1.11±0.49	1.16±0.44	0.93±0.31
[c]$Reff_t$(μm)	0.30±0.10	0.29±0.09	0.30±0.09	0.29±0.10	0.29±0.10	0.29±0.09	0.30±0.10
[c]$Reff_{fine}$(μm)	0.16±0.04	0.16±0.03	0.17±0.04	0.16±0.04	0.16±0.04	0.17±0.04	0.17±0.04
[c]$Reff_{coarse}$(μm)	2.21±0.40	2.26±0.35	2.30±0.39	2.24±0.44	2.19±0.41	2.16±0.39	2.27±0.42
[c]Volume($\mu m^3/\mu m^2$)	0.19±0.09	0.19±0.09	0.19±0.09	0.18±0.09	0.17±0.09	0.18±0.09	0.17±0.07
[c]$Volume_{fine}$($\mu m^3/\mu m^2$)	0.10±0.06	0.11±0.06	0.11±0.07	0.10±0.06	0.10±0.06	0.10±0.06	0.10±0.06
[c]$Volume_{coarse}$($\mu m^3/\mu m^2$)	0.09±0.06	0.08±0.05	0.08±0.06	0.08±0.05	0.08±0.06	0.08±0.07	0.07±0.05
[c]DARF-BOT(W/m^2)	−93±44	−84±41	−80±40	−81±39	−79±39	−82±40	−74±34
[c]DARF-TOA(W/m^2)	−35±20	−36±21	−37±21	−36±21	−35±20	−35±21	−40±19

306 Table 1 (Continued)

307 [a] Number of available observation days.

308 [b] Number of instantaneous observations.

309 [c] Optical parameters at a wavelength of 440 nm.

310 [d] Angström exponents between 440 and 870 nm.

311 [e] Optical parameters at a wavelength of 670 nm.

312 [f] Optical parameters at a wavelength of 870 nm.

313 [g] Optical parameters at a wavelength of 1020 nm.

314

Unlike one peak $AOD_{440\ nm}$ distribution found in June–August over northern and northeastern China (Che et al., 2015), the monthly averaged AODs at 440 nm at all seven sites showed two peaks, one in June and the other in September (Fig.3) with mean values of ~1.26 ± 0.50 (FMF ~ 0.93) and ~1.03 ± 0.57 (FMF ~ 0.95), respectively. The FMF is defined as the fine mode particle AOD_{440nm} fraction ($AOD_{fine(440nm)}/AOD_{440nm}$). Low $AOD_{440\ nm}$ values of ~0.40 - 0.60 were found in July and August throughout the region, and these low values are consistent with the discussion above concerning aerosol microphysical characteristics. That is, hygroscopic effects and/or cloud processing of fine-mode aerosol particles caused greater extinction in June and September compared with July and August. Zhang et al. (2015) reported the hygroscopic particles under high relative humidity conditions could cause strong aerosol light scattering in the Yangtze River Delta. Other meteorological factors also may have played a role in the variations in $AOD_{440\ nm}$ during summer because in July and August, subtropical high-pressure systems prevail, and the planetary boundary layer (PBLH) at Hangzhou is deep, ~1.5–2.0 km (Sun et al., 2017). The large PBLH associated with subtropical anticyclone favor aerosol dispersion, and this can help explain the relatively low aerosol extinction observed in July and August. In January and February, high $AOD_{440\ nm}$ values (0.71-0.89) were observed at all sites, and this can be attributed to emissions from residential heating and the stability of the atmosphere, which can cause the near surface accumulation of aerosol particles. The high $AOD_{440\ nm}$ values in winter also are consistent with studies by Cao et al. (2009) who reported that the PM_{10} mass concentrations at Hangzhou were highest in winter. According to the PM_{10} mass concentration measurements during 2012-2015 at Hangzhou, it was found that the PM_{10} mass concentrations was about 82.2 ± 9.5, 59.1 ± 6.0, 82.8 ± 13.9, and 92.3 ± 14.3 μg/m^3 in spring, summer, autumn, and winter, respectively (see the supplement).

The extinction Angström exponent (EAE = $-d\ln[EAOD(\lambda)]/d\ln(\lambda)$) can be regarded as an indicator of aerosol size; that is, $EAE_{440\ nm\text{-}870\ nm} > 1.00$ typically indicates that the aerosol particles are small. The mean extinction Angström exponent at all seven CARSNET sites was higher than 1.20 throughout the year (Table 1), which means that small particles were predominant. This finding is consistent with the reported dominance of small particles from

anthropogenic emissions and agricultural activity in the region (Tan et al., 2009).

3.3 Aerosol optical properties: single-scattering albedo

The SSAs at 440 nm at our seven sites in YRD region varied from 0.91 to 0.94 (Table 1), and boxplots of the monthly SSAs at wavelengths of 440, 670, 870 and 1020 nm are shown in Figure 4. Eck et al. (2005) reported that the SSAs at 440 nm from AERONET retrievals were confined to a relatively narrow range of values globally from ~0.82 to 0.98. Therefore, the SSA values in this study may be explained by moderately to strongly absorbing aerosols from industrial emissions and other anthropogenic sources. The $SSA_{440\ nm}$ at Hangzhou site was 0.91 ± 0.06, which is lower than that at the rural ChunAn site (0.94 ± 0.03). As Dubovik et al. (2000, 2002, 2006) reported, the SSA depends on two factors—particle size and composition. From Table 1, one can see that the differences in effective radii for total, fine and coarse mode particles between Hangzhou and ChunAn are quite small, and therefore, the differences in SSAs between the two sites can best be explained by differences in composition. Furthermore, the differences in SSAs between these sites indicate that there was a higher percentage of absorbing aerosols at urban site than the rural one.

The SSAs for seven sites showed significant month-to-month variations. The increased scattering (light-absorbing) effects seen in June can be attributed to hygroscopic growth, which can modify aerosol properties greatly (Xia et al., 2007). The presence of light-absorbing dust aerosols in spring and absorbing aerosols from biomass burning in August were probably responsible for the differences in SSA values observed between those months because of the distinct differences in the intensive optical properties of dust and biomass burning products (Yang et al., 2009). At Hangzhou, the monthly average SSA values at 440 nm were relatively high in February (~0.94 ± 0.05) and June (~0.92 ± 0.06) and more moderate in March (~0.90 ± 0.06) and August (~0.89 ± 0.09). In comparison, the differences in monthly SSA values at the rural ChunAn site were smaller, only varying from 0.92 to 0.95. We conclude from the temporal patterns of the SSAs that the types of aerosols at the urban/suburban sites were more variable than at the rural sites.

The SSA wavelength dependence is a function of the specific absorption/scattering properties of different aerosol types (Sokolik and Toon, 1999; Eck et al., 2010). The SSA for mineral dust particles typically shows a strong wavelength dependence from 440 to 1020 nm with a low value at 440 nm due to iron oxide absorption (Cheng et al., 2006; Dubovik et al., 2002). In spring, especially in March, the SSA was obviously lower at shorter wavelengths than at the longer ones, and this implies absorption by dust particles. This conclusion is consistent with the discussion above concerning the impact of dust on aerosol size distributions. In addition, there was a significant decrease in SSA at shorter wavelengths in July and August at most sites, and this supports the presence of aerosol particles with strong absorption, especially at infrared wavelengths. The decreases in those months can be explained by strongly absorbing aerosols from biomass burning or possibly industrial emissions. As Ding et al. (2013a, b) and Wang and Zhang (2008) have reported, plumes from agricultural burning typically contain light-absorbing carbonaceous aerosols, and these pollutants can seriously impair air quality. Indeed, aerosols from biomass burning were more than likely responsible for the low in SSAs found in our study during July and August.

3.4 Aerosol optical properties: AAOD and AAE

The AAODs at 440 nm at the seven sites were similar ~ 0.04-0.06 (Fig. 5a and Table 1), and therefore, absorbing aerosols apparently were widely distributed throughout the YRD. There were large uncertainties in the $AAOD_{440\ nm}$, however; in fact, the standard deviations (0.03 to 0.05) were comparable to the means, and this reflects the large temporal variability in absorbing aerosol particle loadings. The average $AAOD_{440\ nm}$ at Hangzhou was about 0.02 higher than that at ChunAn, and this shows that the relative proportion of absorbing particles at the urban area was larger than at the rural site, presumably due to greater anthropogenic emissions. From Fig. 5, one can see that the monthly $AAOD_{440\ nm}$ at the urban sites from March to November usually exceeded 0.05, which implies there were more absorbing species in spring and autumn compared with winter (December to February) when the $AAOD_{440\ nm}$ tended to be lower, < 0.05. This result suggests that the relative abundances of light-absorbing particles were lower in winter compared with other seasons, and this is different from many

399 regions in northern China where the AAODs are highest in winter due to the emission of
400 absorbing particles from residential heating and other sources (Zhao et al., 2015). At the
401 ChunAn, the variations in AAODs were smoother than the more heavily impacted urban sites,
402 and the monthly mean AAODs at ChunAn were < 0.05 throughout the year.

403 The AAE can be viewed as an indicator of the type of dominant absorbing aerosol
404 particles, which include black carbon, organic matter, and mineral dust (Giles et al., 2012).
405 Generally, an AAE < 1 indicates mixing, coating, and coagulation of black carbon with organic
406 and inorganic materials; an AAE close to 1 indicates absorbing black carbon aerosols from the
407 fossil fuel burning; and an AAE >1.10 indicates absorbing aerosols mainly from the biomass
408 burning or mineral dust (Russell et al., 2010; Bergstrom et al., 2007; Lack and Cappa, 2010).
409 The annual mean AAEs at Hangzhou, Xiaoshan, Fuyang, LinAn, Tonglu, Jiande and ChunAn
410 were 1.13 ± 0.46, 0.88 ± 0.42, 0.85 ± 0.43, 0.98 ± 0.35, 1.11 ± 0.49, 1.16 ± 0.44 and 0.93 ±
411 0.31, respectively (Table 1), and for discussion purposes, the seven sites were grouped into
412 three categories based on their average AAEs. The mean AAE values at Xiaoshan and
413 Fuyang were < 1.00, which suggests that coated black carbon particles dominated at these
414 two sites. However, this also could be due to measurement uncertainties due to smaller
415 numbers of samples from those sites or to slightly larger values of the imaginary part of the
416 refractive index at longer wavelengths for certain particles (Bergstrom et al., 2007). There
417 would need to more observations to confirm the low AAEs at these two sites.

418 The AAE values ~1.00 at LinAn and ChunAn indicate that the absorbing aerosol
419 population was mainly composed of black carbon from fossil fuel burning. LinAn has a more
420 developed economy compared with Tonglu and Jiande, and in comparison, LinAn has many
421 more motor vehicles and is more heavily impacted by industrial emissions and fossil fuel
422 combustion. In contrast, the ChunAn site is located in the Qiandao Lake National Water
423 Resources Protection Zone where biomass burning and industrial activities are banned. Thus,
424 emissions from motor vehicles are probably the main source of absorbing carbon aerosols at
425 ChunAn. Finally, the AAE values at Hangzhou, Tonglu and Jiande were > 1.10, indicating a
426 predominance of light-absorbing aerosols from either biomass burning or mineral dust.

Hangzhou has a population of ~10 million and more than one million vehicles, and the city can be impacted by fugitive dust and biomass burning emissions (Cao et al., 2009). Tonglu and Jiande have small economies compared with Hangzhou, but there is more agricultural production near those two sites, and they can be impacted by biomass burning. These inter-site differences in the AAEs reflect a degree of spatial heterogeneity in the distributions of absorbing aerosols even though the AODs were relatively similar, and these differences likely result from the many types of emission sources that can impact the sites.

3.5 Direct Aerosol radiative forcing at the Earth's surface and TOA

In this study, only clear sky direct aerosol radiative forcings could investigated because the aerosol microphysical and optical parameters were derived from ground-based retrievals under free cloud conditions. For the direct aerosol radiative forcing calculations, the solar fluxes are only evaluated for solar zenith angles (SZA) between 50º and 80º, which is where the solar geometry conditions are the most appropriate for retrieving the aerosol properties (Dubovik et al., 2000, 2002).

The annual direct DARF-BOA values under clear conditions for Hangzhou, Xiaoshan, Fuyang, LinAn, Tonglu, Jiande and ChunAn were −93 ± 44, −84 ± 40, −80 ± 40, −81 ± 39, −79 ± 39, −82 ± 40 and −74 ± 34 W/m^2, respectively (Figure 6a). The DARF-BOA at Hangzhou was ~ −20 W/m^2 lower than that at the rural ChunAn site. The DARFs at the Earth's surface and TOA are governed by the aerosol microphysical and optical properties, primarily particle size distributions, AODs and SSAs. The large negative DARF-BOA values at Hangzhou can be attributed to the high aerosol extinction ($AOD_{440\ nm}$ ~ 0.76) and small absorption (SSA at 440 nm ~0.91). These calculations indicate that effects of those particles on radiative fluxes can cause significant surface cooling at that urban site. In comparison, at the rural ChunAn site, less negative DARF-BOA values result from lower aerosol extinction ($AOD_{440\ nm}$ ~ 0.68) and higher scattering ($SSA_{440\ nm}$ ~ 0.94).

The monthly DARF-BOA at the seven sites was most strongly negative in June, followed by March and September. The strong cooling effect at the surface in June was due to the high aerosol extinction (in section 3.2) and in particular the high volumes of fine-mode particles as

shown in Fig.2. Weakly absorbing particles with $SSA_{440\ nm}$ ~0.90-0.95 (Fig.6) also would reduce the flux of solar radiation to the surface. A large surface cooling effect also was found in March and April. Although the AOD in spring was lower than in winter, there were more strongly absorbing aerosols with relatively smaller SSAs at shorter wavelengths then, and this can be attributed to the presence of mineral aerosol particles. These coarse mode particles with high volumes and large radii are common in spring (see section 3.1), and they can absorb and scatter solar radiation and in so doing cool the surface. Surface cooling in September can be explained by high aerosol extinction that resulted from the high volumes of weakly absorbing fine-mode particles ($SSA_{440\ nm}$ ~0.90-0.95). These results indicate that the attenuation of the solar radiation by the aerosols leads to significant surface cooling over the YRD.

The DARF-TOA annual mean values under clear conditions were ~ −40 W/m^2 at all sites (Figure 7a), and these negative DARF-TOA values indicate that the aerosols caused cooling whole earth-atmosphere system in the YRD. This is different from the case in north/northeastern China where the instantaneous DARF-TOA value can be positive in winter due to the high surface reflectance of short wavelength radiation combined with atmospheric heating caused by absorbing aerosols (Zhao et al., 2015, Che et al., 2014).

The monthly DARF-TOA means under clear conditions varied smoothly during two periods: (1) from January to May, (2) from October to December (Fig. 7). The DARF-TOA values were found approximate -40 W/m^2 at all sites in above two periods. However, the monthly DARF-TOA means in June and September exceeded -40 W/m^2 at most sites, which indicated more cooling effects on the whole earth-atmosphere system due to large aerosol extinctions in YRD. The DARF-TOA means were about −20 W/m^2 at the seven sites in July/August, which suggests weak cooling at that time. In contrast, the DARF-TOA values under clear conditions at Shenyang (urban area of Northeastern China), Beijing (urban area of Northern China), and Xianghe (rural area of Northern China) showed the negative peak during June to August due to the large aerosol extinctions in summer season (Zhao et al., 2015; Xia et al., 2016). As noted in section 3.3, the SSA was low in July and August, and that was

attributed to absorbing particles from biomass burning. Ding et al. (2016) found that large quantities of black carbon can be emitted from biomass burning in the YRD during the summer, and because these particles strongly absorb at infrared wavelengths, they can cause heating up the atmosphere and resulting in lower negative ARF-TOA. Indeed, the positive DARF-TOA we found under clear conditions from April to October were mainly due to the effects of strongly absorbing particles; that is, the SSAs at 440 nm were < 0.80, and they showed a strong decrease with wavelength (not shown here) when DARF-TOA values were positive. Moreover, strongly absorbing aerosol particles can heat the atmosphere column and the TOA at the same time.

3.6 Aerosol type classification based on the aerosol optical properties

In previous studies, aerosol types have sometimes been simply classified as dust (high AOD, low AE) and anthropogenic aerosols (high AOD, high AE) (Che et al., 2009a, b; Wang et al., 2010). However, aerosol direct radiative forcing is affected by the absorptivity of aerosol and the underlying surface conditions (Haywood and Shine, 1995), and there are advantages to better characterization of the aerosol populations. For example, the classification of ground-based aerosol types can be used to compare and validate aerosol types in chemical transport models and satellites retrievals (Lee et al., 2010). Thus, it is advantageous to categorize aerosols as absorbing or non-absorbing based on ground-based optical parameters, including SSA, fine-mode fraction of AOD, and EAE etc. In this study, we used the SSA, FMF, and EAE values to classify the fine and coarse mode particles from each site into eight groups of particles following the method of Zheng et al. (2017). The eight types of particles were (I) highly-absorbing fine-mode particles (AE > 1.2, SSA ≤ 0.85); (II) moderately-absorbing fine-mode particles (AE > 1.2, 0.85 ≤ SSA < 0.9); (III) slightly-absorbing fine-mode particles (AE > 1.2, 0.9 ≤ SSA < 0.95); (IV) weakly-absorbing fine-mode particles (AE > 1.2, SSA > 0.95); (V) mixed-absorbing particles (0.6 ≤ AE < 1.2, SSA ≤ 0.95); (VI) mixed slightly absorbing particles (0.6 ≤ AE < 1.2, SSA > 0.95); (VII) strongly absorbing coarse mode particles—mainly dust (AE≤ 0.6, SSA ≤ 0.95); (VIII) weakly-absorbing coarse-mode particles (AE ≤ 0.6, SSA > 0.95).

From Figure 8 and 9, one can see that the absorbing fine-mode particles (Type I, II and III) accounted for ~30 to 50% of the aerosol in the YRD region with the FMF ~0.86-0.94%. The percentages of “highly-absorbing fine-particles” (Type I) was obviously larger at Hangzhou (~8%) (FMF~0.90) than the smaller city sites (~2-3%), and at the ChunAn rural site, the percentages of Type I particles was only ~0.16% (FMF~0.91). This indicates that there were greater emissions of strong absorbing aerosols from sources such as biomass burning and/or urban/industrial activities at the urban site compared with the rural one. The proportion of weakly-absorbing fine-mode particles (Type IV) varied from ~20 to 30% for all sites, and the FMF varies from 0.89~0.95 at same time, which suggests the second largest aerosol type in the area is weakly-absorbing fine-mode particles. The percentage of mixed absorbing particle (Type V) was about ~25-26% both at Hangzhou and the rural ChunAn site, which is slightly higher than that at small city sites (~10-20%) where the FMF of these particles was ~0.81-0.89. The higher FMF at Hangzhou was probably due to the complex aerosol emission sources that impact that megacity while at ChunAn, which is surrounded by mountains, the basin topography promotes particle mixing. The mixed slightly absorbing particles (Type VI) showed the highest percentages of the total aerosol number at Fuyang (18.05%) and ChunAn (15.32%), and the FMF of this group varied from 0.84-0.91 at all sites. The contribution of Type VI mixed slightly absorbing particles at Hangzhou was ~11.49%, and the FMF (0.86) there was not as high as at ChunAn (0.91). The proportion of strongly absorbing coarse mode particles—mainly dust (Group VII) was only ~1.04% of the total particle count at Hangzhou while at the other sites the percent abundances were < 1%, and the FMF for these particles were ~0.50-0.63 at all sites. These patterns show that the YRD region is different from regions in north China, including Beijing, where dust particles contribute significantly to the coarse mode absorption (Zheng et al., 2017). The percentage of weakly-absorbing coarse–mode particles (Group VIII) at all sites was < 0.54%, which shows that this aerosol type was rare. In addition, the FMF of Group VIII particles was 0.5–0.8 with large uncertainties at all sites. Overall, this analysis of aerosol types shows that the aerosol absorption is relatively weak in the YRD region, and the fine-mode makes up an especially large contribution of the absorbing

particles at Hangzhou.

3.7 Discussion

Compared with previous studies on the climatology of aerosol microphysical and optical properties in China, large volumes and effective radii of fine-mode aerosol, as well as high AODs at 440 nm were found at most sites in June and September but not in July or August. This is remarkably different from studies conducted in Northeastern/Northern China where these properties showed the maximum values in July or August (Eck et al., 2005; Zhao et al., 2013; Che et al., 2015b). This reflects the distinctive climatology of aerosol microphysical and optical properties in the YRD region of Eastern China. This information on the distributions and variations of aerosol microphysical and optical properties obtained in our study should be taken into account in the validation of satellite retrievals and aerosol modeling studies in the future.

The $AOD_{440\ nm}$ values in our study (0.71- 0.76) are similar to other urban areas of China, such as Shenyang (0.75), Beijing (0.76), Tianjin (0.74), Shanghai (0.70), and Hefei (0.69) (Pan et al., 2010; He et al., 2012; Zhao et al., 2013; Che et al., 2015b, Liu et al., 2017). This indicates that high aerosol loadings caused by anthropogenic activities occur over many urban, suburban, and even rural areas of eastern China. The $AOD_{440\ nm}$ at the rural ChunAn site (~0.68) is ~ 2–6 times higher than in other rural sites in China, such as Longfengshan (0.35; northeastern China), Xinglong (0.28, northern China), Akedala (0.20, northwestern China) and Shangri-La (0.11, southwestern China) (Wang et al., 2010; Che et al., 2011; Zhu et al., 2014; Che et al., 2015b). Therefore, strong aerosol effects on light extinction occur not only in urban areas but also in much or possibly all of the YRD. The $SSA_{440\ nm}$ in our study ranged from 0.91–0.94, which is similar to other regions of China, such as Wuhan (0.92), Beijing (0.89) and Xinglong (0.92) (Wang et al., 2015; Xin et al., 2014; Zhu et al., 2014); this suggests aerosol particles in the YRD are slight to relatively strong absorbers of violet/indigo wavelengths.

Although the AAE has been used as an indicator of the dominant absorbing aerosol type, the SSA, FMF, and EAE also used to classify the absorption characteristics of fine and coarse

mode particles. It should also be mentioned that uncertainties in the AAE calculations due to uncertainties in the SSAs may have contributed to the observed differences between sites (Bergstrom et al., 2007; Giles et al. 2011). Ideally, the aerosol physical and chemical characteristic measurements will be combined at some point to more definitively classify the aerosol types. In addition, even though Zhuang et al. (2017) pointed that the DARFs are not very sensitive to vertical profiles under clear sky condition, future research should take into account the vertical distributions of aerosols to more accurately assess the direct aerosol radiative forcing effects.

The useful observations at most sites in this study were made on 439~562 days, but smaller numbers of observation were made in Xiaoshan and Fuyang because of instrument failures, 180 and 217 days, respectively. There were fewer than 15 days of useful data for October and November at Fuyang, and for June, July, September, and November at Xiaoshan. While the available data do provide insights into the aerosol characteristics at the sites, more extended observations should be conducted at the two sites in future.

4. Conclusions

A detailed study of aerosol microphysical and optical properties retrieved from synchronous ground-based sun photometer observations was conducted at seven sites in the Yangtze River Delta region of Eastern China from 2011 to 2015. The aerosol were classified into eight types, and calculations were made for the direct aerosol radiative forcing (DARF) at the top and bottom of the atmosphere. The conclusions of the study can be summarized as follows:

A relatively homogeneous distribution of aerosol microphysical properties was found for a megacity, five small cities, and a rural site in the YRD region. High particle volumes of coarse-mode aerosol occurred in March to May, which reflects the existence of large mineral particles from springtime dust storms. High volumes and large effective radii of fine-mode aerosol in June and September were found at most sites, and this was attributed to aerosol hygroscopicity and cloud processing. The low volumes and large bandwidth of both fine- and

coarse-mode aerosol found in July and August at all sites was explained by the wet removal of coarse particles during the heavy precipitation in June and the influences of subtropical anticyclones in summer.

The $AOD_{440\ nm}$ generally decreased from the east coast (0.76–Hangzhou) to the inland areas towards the west (0.68–ChunAn), and this can be explained by anthropogenic impacts of the more urbanized regions in the east YRD region. The $AOD_{440\ nm}$ values at urban and rural sites of YRD were 0.68–0.76, and the fine-mode fractions were ~0.90, which indicates that fine-mode particles were more important than the coarse mode for the light extinction. The difference in AODs between the urban and rural sites was less than 10%, and this can be explained by somewhat stronger effects of anthropogenic activities in the urban area. The monthly averaged AODs at 440 nm showed peaks in June and September that resulted from increases fine-mode aerosol particles. However, AODs at 440 nm in July and August were the lowest over the year, and that was related to conditions favorable for aerosol dispersion. The mean extinction Angström exponent was > 1.20 all year indicating that small particles were predominant in the region. The SSAs at 440 nm varied from 0.91 to 0.94 at the urban and rural sites, indicating that the aerosol particles were moderately absorbing, and this is almost surely a result of impacts from the high industrial emissions and other anthropogenic activities in the region. There was an obvious wavelength dependence for the SSA in July and August, and aerosols absorbed most strongly at infrared wavelengths. The AAODs at 440 nm at the seven sites were ~0.04–0.06, which suggests that absorbing aerosols are distributed more-or-less homogeneously throughout the YRD region. The averaged $AAOD_{440\ nm}$ at Hangzhou is about 0.02 higher than that at ChunAn, which indicates the relative proportion of absorbing particles in the urban area is larger compared with the rural area. The $AAOD_{440\ nm}$ in winter was < 0.05, which suggests that light absorption by the particles was low compared with the other seasons. The geographical variability in the distributions of the AAEs suggests that the absorbing aerosols possibly have different optical characteristics related to the local emission sources in the YRD.

The DARF-BOA at Hangzhou was ~ −20 W/m^2 lower than that at the rural ChunAn site,

which shows stronger aerosol cooling at the megacity. The monthly DARF-BOA was strongly negative in June due to the high aerosol extinction and especially the high fine-mode volume. The DARF-TOAs under clear conditions were < −40 W/m^2, but about −20 W/m^2 in July/August which suggests weaker cooling in mid summer. The DARF-TOAs were positive from April to October when the $SSA_{440\ nm}$ < 0.80, and the greater effects at shorter wavelengths was likely due to emissions of carbonaceous particles from the burning of crop residues.

The SSA, FMF, and EAE values were used to classify the particles as absorbing or non-absorbing. Relatively large emissions of strongly absorbing aerosols in the Hangzhou urban area was the result of biomass burning and/or urban/industrial activities. The aerosol type classification showed overall that the aerosol absorption is weak to moderate in the YRD, and the fine-mode has a large contribution to the higher percentage of absorbing particles at the Hangzhou site.

Acknowledgments

This work was supported by grant from National Key R & D Program Pilot Projects of China (2016YFA0601901), National Natural Science Foundation of China (41590874 &41375153), Natural Science Foundation of Zhejiang Province (LY16010006), the CAMS Basis Research Project (2016Z001 & 2014R17), the Climate Change Special Fund of CMA (CCSF201504), CAMS Basic Research Project (2014R17),the Special Project of Doctoral Research supported by Liaoning Provincial Meteorological Bureau (D201501), Hangzhou Science and Technology Innovative project (20150533B17)and the European Union Seventh Framework Programme (FP7/2007-2013) under grant agreement no. 262254. The authors would like to thank the three anonymous reviewers and the editor for their constructive suggestions and comments.

References

Ackerman, P., and Toon, O.B.: Absorption of visible radiation in atmosphere containing mixtures of absorbing and nonabsorbing particles, Appl. Opt., 20, 3661-3668, 1981.

Albrecht, B.: Aerosols, cloud microphysics, and fractional cloudiness, Science, 245,

649 1227-1230, 1989.
650 Bergstrom, R.W., Pilewskie, P., Russell, P.B., Redemann, J., Bond, T.C., Quinn, P.K., and
651 Sierau, B.: Spectral absorption properties of atmospheric aerosols, Atmos. Chem. Phys., 7,
652 5937–5943, doi: 10.5194/ acp-7-5937-2007, 2007.
653 Cao, J., Shen, Z., Chow, J.C., Qi, G., and Watson, J.G.: Seasonal variations and sources of
654 mass and chemical composition for PM10 aerosol in Hangzhou, China, Particuology, 7, 161–
655 168, doi:10.1016/j.partic.2009.01.009, 2009.
656 Charlson, R.J., Schwartz, S.E., Hales, J.M., Cess, D., Coakley, J.A., and Hansen, J.E.:
657 Climate forcing by anthropogenic aerosols, Science, 255, 423–430, 1992.
658 Che, H.Z., Xia, X.A., Zhu, J., Wang, H., Wang, Y.Q., Sun, J.Y., Zhang, X.C., Zhang, X.Y., and
659 Shi, G.Y.: Aerosol optical properties under the condition of heavy haze over an urban site of
660 Beijing, China, Environ. Sci. Pollut. Res., 22, 1043–1053, 2015a.
661 Che, H. Z., Zhang, X. Y., Alfraro, S., Chatenet, B., Gomes, L., and Zhao, J. Q.: Aerosol optical
662 properties and its radiative forcing over Yulin, China in 2001 and 2002, Adv. Atmos. Sci., 26,
663 564–576, doi:10.1007/s00376-009-0564-4, 2009b.
664 Che, H., Zhang, X., Chen, H., Damiri, B., Goloub, P., Li, Z., Zhang, X., Wei, Y., Zhou, H., Dong,
665 F., Li, D., and Zhou, T.: Instrument calibration and aerosol optical depth (AOD) validation of the
666 China Aerosol Remote Sensing Network (CARSNET), J. Geophys. Res., 114, doi:
667 org/10.1029/2008JD011030, 2009a.
668 Che, H., Wang, Y., Sun, J., and Zhang, X.: Assessment of In-situ Langley Calibration of
669 CE-318 Sunphotometer Mt. Waliguan Observatory, China, SOLA, 7, 089-092, doi:
670 10.2151/sola.2011-023, 2011.
671 Che, H.Z., Zhang, X.Y., Xia, X.A., Goloub, P., Holben, B., Zhao, H., Wang, Y., Zhang, X.C.,
672 Wang, H., and Blarel, L. et al.: Ground-based aerosol climatology of China: Aerosol optical
673 depths from the China Aerosol Remote Sensing Network (CARSNET) 2002–2013, Atmos.
674 Chem. Phys., 15, 7619–7652, 2015b.
675 Che, H.Z., Xia, X.A., Zhu, J., Wang, H., Wang, Y.Q., Sun, J.Y., Zhang, X.C., Zhang, X.Y., and
676 Shi, G.Y.: Aerosol optical properties under the condition of heavy haze over anurban site of
677 Beijing, China, Environ. Sci. Pollut. Res.,http://dx.doi.org/10.1007/s11356-014-3415-5, 2014.
678 Cheng, T., Liu, Y., Lu, D., Xu, Y., and Li, H.: Aerosol properties and radiative forcing in

679 Hunshan Dake desert, northern China, Atmos. Environ., 40, 2169-2179, 2006.
680 Cheng, T.T., Xu, C., Duan, J.Y., Wang, Y.F., Leng, C.P., Tao, J., Che, H.Z., He, Q.S., Wu, Y.F.,
681 Zhang, R.J., Li, X., Chen, J.M., Kong, L.D., and Yu, X.N.: Seasonal variation and difference of
682 aerosol optical properties in columnar and surface atmospheres over Shanghai, Atmos.
683 Environ., 123, 315-326, 2015.
684 Ding, A. J., Fu, C. B., Yang, X. Q., Sun, J. N., Zheng, L. F., Xie, Y. N., Herrmann, E., Nie, W.,
685 Petäjä, T., Kerminen, V.-M., and Kulmala, M.: Ozone and fine particle in the western Yangtze
686 River Delta: an overview of 1 yr data at the SORPES station, Atmos. Chem. Phys., 13, 5813–
687 5830, doi:10.5194/acp-13-5813-2013, 2013a.
688 Ding, A. J., Fu, C. B., Yang, X. Q., Sun, J. N., Petäjä, T., Kerminen, V.-M., Wang, T., Xie, Y.,
689 Herrmann, E., Zheng, L. F., Nie, W., Liu, Q., Wei, X. L., and Kulmala, M.: Intense atmospheric
690 pollution modifies weather: a case of mixed biomass burning with fossil fuel combustion
691 pollution in eastern China, Atmos. Chem. Phys., 13, 10545-10554,
692 doi:10.5194/acp-13-10545-2013, 2013b.
693 Ding, A. J., Huang, X., Nie, W., Sun, J. N., Kerminen, V.M., Petäjä, T., Su, H., Cheng, Y. F.,
694 Yang, X.Q., and Wang, M.H. et al.: Enhanced haze pollution by black carbon in megacities in
695 China, Geophys. Res. Lett., 43, 2873–2879, doi: 10.1002/2016GL067745, 2016.
696 Duan, J., Mao, J.: Study on the distribution and variation trends of atmospheric aerosol optical
697 depth over the Yangtze River Delta, Acta Scien. Circum., 27 (4), 537-543, 2007.
698 Dubovik, O., Holben, B.N., Eck, T.F., Smirnov, A., Kaufman, Y.J., King, M.D., Tanre, D.,
699 Slutsker, I.: Variability of absorption and optical properties of key aerosol types observed in
700 worldwide locations, J. Atmos. Sci., 59, 590–608, 2002.
701 Dubovik, O., King, M.D.: A flexible inversion algorithm for retrieval of aerosol optical properties
702 from sun and sky radiance measurements, J. Geophys. Res., 105 (D16), 20673, 2000.
703 Dubovik, O., Sinyuk, A., Lapyonok, T., Holben, B.N., Mishchenko, M., Yang, P., Eck, T.F.,
704 Volten, H., Munoz, O., Veihelmann, B., van der Zande, W.J., Leon, J.F., Sorokin, M., and
705 Slutsker, I.: Application of spheroid models to account for aerosol particle nonsphericity in
706 remote sensing of desert dust, J. Geophys. Res.-Atmos., 111 (D11), 2006.
707 Dubovik, O., Smirnov, A., Holben, B. N., King, M. D., Kaufman, Y. J., Eck, T. F., and Slutsker, I.:
708 Accuracy assessments of aerosol optical properties retrieved from Aerosol Robotic Network
709 (AERONET) Sun and sky radiance measurements, J. Geophys. Res., 105(D8), 9791–9806,

2000.

Dubuisson, P., Buriez, J. C., and Fouquart, Y.: High spectral resolution solar radiative transfer in absorbing and scattering media, application to the satellite simulation, J. Quant. Spectrosc. Radiat. Transfer, 55, 1996.

Eck, T.F., Holben, B.N., Dubovik, O., Smirnov, A., Goloub, P., Chen, H.B., Chatenet, B., Gomes, L., Zhang, X.Y., and Tsay, S.C. et al.: Columnar aerosol optical properties at AERONET sites in central eastern Asia and aerosol transport to the tropical Mid-Pacific, J. Geophys. Res., 110, 2005.

Eck, T. F., Holben, B. N., Reid, J. S., Dubovik, O., Smirnov, A., O'Neill, N. T., Slutsker, I., and Kinne, S.: Wavelength dependence of the optical depth of biomass burning, urban, and desert dust aerosols, J. Geophys. Res., 104(D24), 31333–31349, 1999.

Eck, T.F., Holben, B.N., Reid, J.S., Giles, D.M., Rivas, M.A., Singh, R.P., Tripathi, S.N., Bruegge, C.J., Platnick, S., Arnold, G.T., Krotkov, N.A., Carn, S.A., Sinyuk, A., Dubovik, O., Arola, A., Schafer, J.S., Artaxo, P., Smirnov, A., Chen, H. and Goloub, P.: Fog- and Cloud induced aerosol modification observed by the Aerosol Robotic Network (AERONET), J. Geophys. Res., 117, D07206, doi: 10.1029/2011JD016839, 2012.

Eck, T. F., Holben, B. N., Sinyuk, A., Pinker, R. T., Goloub, P., Chen, H., Chatenet, B., Li, Z., Singh, R. P., and Tripathi, S. N.: Climatological aspects of the optical properties of fine/coarse mode aerosol mixtures, J. Geophys. Res. Atmos. (1984–2012), 115, 19205, 2010.

Estellés, V., Campanelli, M., Utrillas, M. P., Expósito, F., and Martínezlozano, J. A.: Comparison of AERONET and SKYRAD4.2 inversion products retrieved from a Cimel CE318 sunphotometer, Atmos. Meas. Tech., 4, 569-579, 2012.

Fu, Q., Zhuang, G., Wang, J., Xu, C., Huang, K., Li, J., Hou, B., Lu, T., and Streets, D. G.: Mechanism of formation of the heaviest pollution episode ever recorded in the Yangtze River Delta, China, Atmos. Environ., 42, 2023-2036, 2008.

Fu, X., Wang, S.X., Cheng, Z., Xing, J., Zhao, B., Wang, J.D., and Hao, J.M.: Source, transport and impacts of a heavy dust event in the Yangtze River Delta, China, in 2011, Atmos. Chem. Phys., 14, 1239–1254, doi:10.5194/acp-14-1239-2014, 2014.

García, O. E., Díaz, J. P., Expósito, F. J., Díaz, A. M., Dubovik, O., Dubuisson, P., Roger, J.-C., Eck, T. F., Sinyuk, A., Derimian, Y., Dutton, E. G., Schafer, J. S., Holben, B. N., and García, C. A: Validation of AERONET estimates of atmospheric solar fluxes and aerosol

741 radiative forcing by ground-based broadband measurements, J. Geophys. Res., 113, D21207,
742 doi:10.1029/2008JD010211, 2008.
743 García, O. E., Díaz, J. P., Expósito, F. J., Díaz, A. M., Dubovik, O., and Derimian, Y.: Aerosol
744 radiative forcing: AERONET based estimates, climate Models, edited by: Druyan, L., ISBN:
745 978-953-51-0135-2, InTech, 2012.
746 Giles, D. M., Holben, B. N., Tripathi, S. N., Eck, T. F., Newcomb, W. W., Slutsker, I., Dickerson,
747 R. R., Thompson, A. M., Mattoo, S., and Wang, S. H.: Aerosol properties over the
748 Indo-Gangetic Plain: A mesoscale perspective from the TIGERZ experiment, Journal of
749 Geophysical Research Atmospheres, 116, 10--1029, 2011.
750 Giles, D. M., Holben, B. N., Eck, T. F., Sinyuk, A., Smirnov, A., Slutsker, I., Dickerson, R. R.,
751 Thompson, A. M., and Schafer, J. S.: An analysis of AERONET aerosol absorption properties
752 and classifications representative of aerosol source regions, Journal of Geophysical Research
753 Atmospheres, 117, 127-135, 2012.
754 Goloub, P., Li, Z., Dubovik, O., Blarel, L., Podvin, T., Jankowiak, I., Lecoq, R., Deroo, C.,
755 Chatenet, B., and Morel, J. P.: PHOTONS/AERONET sunphotometer network overview:
756 description, activities, results, Fourteenth International Symposium on Atmospheric and Ocean
757 Optics/Atmospheric Physics, 69360V-69360V-69315, 2007.
758 Hansen, J., Sato, M., Ruedy, R., Lacis, A., and Oinas, V.: Global warming in the twenty-first
759 century: an alternative scenario, Proc. Nat. Acad. Sci. USA, 97, 9875-9880, 2000.
760 Haywood, J.M., and Shine, K.P.: The effect of anthropogenic sulfate and soot aerosol on the
761 clear sky planetary radiation budget, Geophys. Res. Lett., 22, 603-606, DOI:
762 10.1029/95GL00075, 1995.
763 He, Q., Li, C., Geng, F., Yang, H., Li, P., Li, T., Liu, D., and Pei, Z.: Aerosol optical properties
764 retrieved from Sun photometer measurements over Shanghai, China, J. Geophys. Res.
765 Atmos., 117, 81-81, 2012.
766 Holben, B. N., Eck, T. F., Slutsker, I., Tanré, D., Buis, J. P., Setzer, A., Vermote, E., Reagan, J.
767 A., Kaufman, Y. J., Nakajima, T., Lavenu, F., Jankowiak, I., and Smirnov, A.: AERONET—A
768 Federated Instrument Network and Data Archive for Aerosol Characterization, Remote
769 Sensing of Environment, 66, 1-16, https://doi.org/10.1016/S0034-4257(98)00031-5, 1998.
770 Holben, B. N., Tanré, D., Smirnov, A., Eck, T. F., Slutsker, I., Abuhassan, N., Newcomb, W. W.,
771 Schafer, J. S., Chatenet, B., and Lavenu, F.: An emerging ground-based aerosol climatology:
772 Aerosol optical depth from AERONET, J. Geophys. Res. Atmos., 106, 12067–12097, 2001.

773 Holben, B. N., Kim, J., Sano, I., Mukai, S., Eck, T. F., Giles, D. M., Schafer, J. S., Sinyuk, A.,
774 Slutsker, I., Smirnov, A., Sorokin, M., Anderson, B. E., Che, H., Choi, M., Crawford, J. E.,
775 Ferrare, R. A., Garay, M. J., Jeong, U., Kim, M., Kim, W., Knox, N., Li, Z., Lim, H. S., Liu, Y.,
776 Maring, H., Nakata, M., Pickering, K. E., Piketh, S., Redemenn, J., Reid, J. S., Salinas, S., Seo,
777 S., Tan, F., Tripathi, S. N., Toon, O. B., and Xiao, Q.: An overview of meso-scale aerosol
778 processes, comparison and validation studies from DRAGON networks, Atmos. Chem. Phys.
779 Discuss., https://doi.org/10.5194/acp-2016-1182, in review, 2017.
780 Huang, X., Ding, A., Liu, L., Liu, Q., Ding, K., Niu, X., Nie, W., Xu, Z., Chi, X., Wang, M., Sun, J.,
781 Guo, W., and Fu, C.: Effects of aerosol–radiation interaction on precipitation during
782 biomass-burning season in East China, Atmos. Chem. Phys., 16, 10063-10082,
783 doi:10.5194/acp-16-10063-2016, 2016.
784 Intergovernmental Panel on Climate Change (IPCC).Climate Change 2013. The Scientific
785 Basis; Cambridge University Press: New York, NY, USA, 2013.
786 Kaufman, Y. J., Tanré, D., and Boucher, O. A.: satellite view of aerosols in the climate system,
787 Nature, 419, 215–223, 2002.
788 Lacis, A. A., and Oinas, V.: A description of the correlated kdistribution method for modeling
789 nongray gaseous absorption, thermal emission, and multiple scattering in vertically
790 inhomogeneous atmospheres, J. Geophys. Res., 96, 9027–9063, 1991.
791 Lack, D. A., and Cappa, C. D.: Impact of brown and clear carbon on light absorption
792 enhancement, single scatter albedo and absorption wavelength dependence of black carbon,
793 Atmos. Chem. Phys., 10(9), 4207-4220, 2010.
794 Lee, K. H., Li, Z., Cribb, M. C., Liu, J., Wang, L., Zheng, Y., Xia, X., Chen, H., and Li, B.:
795 Aerosol optical depth measurements in eastern China and a new calibration method, J.
796 Geophys. Res., 115, 4038-4044, doi: 10.1029/2009JD012812, 2010.
797 Lee, J., Kim, J., Song, C.H., Kim, S.B., Chun, Y., Sohn, B.J., and Holben, B.N.: Characteristics
798 of aerosol types from AERONET sunphotometer measurements, Atmos. Environ., 44, 3110–
799 3117, http://dx.doi.org/10.1016/j.atmosenv.2010.05.035, 2010.
800 Li, J., Carlson, B. E., and Lacis, A. A.: Using single-scattering albedo spectral curvature to
801 characterize East Asian aerosol mixtures, J. Geophys. Res. Atmos., 120, 2037–2052, 2015a.
802 Li, S., Wang T., Xie M., Han Y., and Zhuang B.: Observed aerosol optical depth and angstrom

803 exponent in urban area of Nanjing, China, Atmos. Environ., 123, 350–356, 2015b.
804 Li, W.J., Shao, L.Y., and Buseck, P.R.: Haze types in Beijing and the influence of agricultural
805 biomass burning, Atmos. Chem. Phys. 10, 8119–8130, 2010.
806 Li, W.J., Sun, J.X., Xu, L., Shi, Z.B., Riemer, N., Sun, Y.L., Fu, P.Q., Zhang, J.C., Lin, Y.T.,
807 Wang, X.F., Shao, L.Y., Chen, J.M., Zhang, X.Y., Wang, Z. F. and Wang, W.X.: A conceptual
808 framework for mixing structures in individual aerosol particles, J. Geophys. Res., 121,
809 13205-13798, doi:10.1002/2016JD025252, 2016.
810 Li, Z.Q., Eck,T., Zhang, Y., Zhang, Y.H., Li, D.H., Li, L., Xu, H., Hou, W.Z., Lv, Y., Goloub, P. and
811 Gu, X.F.: Observations of residual submicron fine aerosol particles related to cloud and fog
812 processing during a major pollution event in Beijing, Atmos. Environ., 86, 187–192, 2014.
813 Li Z., Lau, W.K.-M., Ramanathan,V., Wu,G., Ding,Y., Manoj,M.G., Liu,J., Qian,Y., Li,J., Zhou,T.,
814 Fan,J., Rosenfeld,D., Ming,Y., Wang,Y., Huang,J., Wang,B., Xu,X., Lee,S.-S., Cribb,M.,
815 Zhang,F., Yang,X.,Takemura, Wang,K., Xia,X., Yin,Y., Zhang,H.,Guo,J.,Zhai,P.M.,
816 Sugimoto,N.,Babu,S. S., and Brasseur,G.P.: Aerosol and monsoon climate interactions over
817 Asia, Rev. Geophys., doi:10.1002/2015RG000500, 2016.
818 Liu, Q.,Ding, W.D.,Xie, L.,Zhang, J.Q.,Zhu, J.,Xia, X.A.,Liu, D.Y.,Yuan, R.M., and Fu, Y.F.:
819 Aerosol properties over an urban site in central East China derived from ground
820 sun-photometer measurements, Sci. China Earth Sci., 60, 297–314,doi:
821 10.1007/s11430-016-0104-3, 2017.
822 Myhre, G.: Consistency between satellite-derived and modeled estimates of the direct aerosol
823 effect, Science, 325, 187–190, 2009
824 Nakajima, T., and Tanaka, M.: Algorithms for radiative intensity calculations in moderately thick
825 atmospheres using a truncation approximation, J. Quant. Spectrosc. Radiat. Transfer, 40, 51–
826 69, 1988.
827 Pan, L., Che, H., Geng, F., Xia, X., Wang, Y., Zhu, C., Chen,M., Gao,W., and Guo, J.: Aerosol
828 optical properties based on ground measurements over the Chinese Yangtze Delta Region,
829 Atmos. Environ., 44(21), 2587-2596, 2010.
830 Panicker, A.S., Lee, D.I., Kumkar, Y.V., Kim, D., Maki, M., Uyeda, H.: Decadal climatological
831 trends of aerosoloptical parameters over three different environments in South Korea., Int. J.
832 Climatol., 33, 1909–1916, 2013.

833 Pappalardo, G., Amodeo, A., Apituley, A., Comeron, A., Freudenthaler, V., Linné, H., Ansmann,
834 A., Bösenberg, J., D'Amico, G., Mattis, I. Mona, L., Wandinger, U., Amiridis,V.,
835 Alados-Arboledas, L., Nicolae, D., and Wiegner, W.: EARLINET: Towards an advanced
836 sustainable European aerosol Lidar network, Atmos. Meas. Tech., 7, 2389–2409, 2014.
837 Roger, J.-C., Mallet, M., Dubuisson, P., Cachier, H., Vermote, E., Dubovik, O., and Despiau, S.:
838 A synergetic approach for estimating the local direct aerosol forcing:applications to an urban
839 zone during the ESCOMPTE experiment, J. Geophys. Res., 111, D13208,
840 http://dx.doi.org/10.1029/2005JD006361, 2006.
841 Russell, P.B., Bergstrom, R.W., Shinozuka, Y., Clarke, A.D., DeCarlo, P.F., Jimenez, J.L.,
842 Livingston, J.M., Redemann, J., Dubovik, O., and Strawa, A.: Absorption Angstrom exponent
843 in AERONET and related data as an indicator of aerosol composition, Atmos.Chem. Phys., 10,
844 1155–1169, http://dx.doi.org/10.5194/acp-10-1155-2010, 2010.
845 Saha, A., and Moorthy, K. K.: Impact of precipitation on aerosol spectral optical depth and
846 retrieved size distributions: A case study, Journal of Applied Meteorology, 43, 902-914, 2004.
847 Sanap, S.D., and Pandithurai, G.: Inter-annual variability of aerosols and its relationship with
848 regional climate over Indian subcontinent, Int. J. Climatol., 35, 1041–1053,
849 http://dx.doi.org/10.1002/joc.4037, 2014.
850 Schwartz, S.E., and Andreae, M.O.: Uncertainty in climate change caused by aerosols,
851 Science, 272, 1121–1122, 1996.
852 Shen X. J., Sun, J. Y., Zhang, X. Y., Zhang, Y. M., Zhang L., Che, H. C., Ma, Q. L., Yu, X. M.,
853 Yue, Y. and Zhang, Y. W.: Characterization of submicron aerosols and effect on visibility during
854 a severe haze-fog episode in Yangtze River Delta, China, Atmospheric Environment, 120,
855 307-316, 2015.
856 Smirnov, A., Holben, B.N., Eck, T.F., Dubovik, O., and Slutsker, I.: Cloud screening and quality
857 control algorithmsfor the AERONET data base, Remote Sens. Environ., 73, 337–349, 2000.
858 Smirnov, A., Holben, B. N., Lyapustin, A., Slutsker, I., and Eck, T. F.: AERONET processing
859 algorithms refinement, AERONET Workshop, May 10– 14, 2004, El Arenosillo, Spain, 2004.
860 Sokolik, I. N., and Toon, O. B.: Incorporation of mineralogical composition into models of the
861 radiative properties of mineral aerosol from UV to IR wavelengths, J. Geophys. Res., 104(D8),
862 9423-9444, doi:10.1029/ 1998JD200048, 1999.
863 Solomon, S., Qin, D., Manning, M., Chen, Z., Marquis, M., Averyt, K.B.,Tignor, M., Miller, and
864 H.L.(Eds.): Climate change 2007: the physical science basis., Contribution of Working Group I

865 to the Fourth Assessment Report of the Intergovernmental Panel on Climate Change.
866 Cambridge University Press, Cambridge, United Kingdom and New York, USA, 2007.
867 Stamnes, K., Tsay, S.C., Wiscombe, W., and Jayaweera, K.: Numerically stable algorithm for
868 discrete-ordinate-method radiative transfer in multiple scattering and emitting layered media,
869 Appl. Opt., 27, 2502–2509, 1988.
870 Sun, Y., Sun, X., Yin, Y., and Han, Y.: Observation Study of Aerosol over Mid-Western North
871 China Plain in Autumn (October), Plateau Meteorology, 32, 1308-1320,
872 10.7522/j.issn.1000-0534.2012.00123, 2013 (in Chinese).
873 Sun, T., Che, H., Qi, B., Wang, Y., Dong, Y., Xia, X., Wang, H., Gui, K., Zheng, Y., Zhao, H., Ma,
874 Q., Du, R., and Zhang, X.: Aerosol optical characteristics and their vertical distributions under
875 enhanced haze pollution events: effect of the regional transport of different aerosol types over
876 eastern China, Atmos. Chem. Phys. Discuss., https://doi.org/10.5194/acp-2017-805, 2017.
877 Takamura, T., and Nakajima, T.: Overview of SKYNET and its activities, Opt. Puray. Apl., 37,
878 3303–3308, 2004.
879 Tan, H., Wu, D., Deng, X., Bi, X., Li, F., and Deng, T.: Observation of aerosol optical depth over
880 the Pearl River Delta, Acta Sci. Circum., 29, 1146–1155, 2009 (in Chinese).
881 Twomey, S.A., Piepgrass, M., and Wolfe, T.L.: An assessment of the impact of pollution on the
882 global cloud albedo, Tellus., 36B, 356-366, 1984.
883 Wang, L.C., Gong, W., Xia, X.A., Zhu, J., Li, J., and Zhu, Z.M.: Long-term observations of
884 aerosol optical properties at Wuhan, an urban site in Central China, Atmos. Environ.,101, 94–
885 102, 2015.
886 Wang, P., Che, H.Z., Zhang, X.C., Song, Q.L., Wang, Y.Q., Zhang, Z.H., Dai, X., and Yu, D.J.:
887 Aerosol opticalproperties of regional background atmosphere in Northeast China, Atmos.
888 Environ., 44, 4404–4412, 2010.
889 Wang, S., and Zhang, C.: Spatial and temporal distribution of air pollutant emissions from open
890 burning of crop residues in China, Sciencepaper Online, 3, 329–333, 2008 (in Chinese).
891 Wang, Z., Liu, D., Wang, Y., Wang, Z., and Shi, G.: Diurnal aerosol variations do affect daily
892 averaged radiative forcing under heavy aerosol loading observed in Hefei, China, Atmos.
893 Meas. Tech., 8, 2901, 2015.
894 Wehrli, C.: Calibration of filter radiometers for the GAW Aerosol Optical Depth network at

Jungfraujoch and Mauna Loa. In: Proceedings of ARJ Workshop, SANW Congress, Davos, Switzerland, pp. 70-71,2002.

Xia, X., Chen, H., Goloub, P., Zong, X., Zhang, W., and Wang, P.: Climatological aspects of aerosol opticalproperties in North China Plain based on ground and satellite remote-sensing data, J. Quant. Spectrosc. Radiat.Transf., 127, 12–23, 2013.

Xia, X., Li, Z., Holben, B., Wang, P., Eck, T., Chen, H., Cribb, M., and Zhao, Y.: Aerosol optical properties and radiative effects in the Yangtze Delta region of China, J. Geophys. Res., 112, D22S12, doi:10.1029/2007JD008859, 2007.

Xia, X., Che, H., Zhu, J., Chen, H., Cong, Z., Deng, X., Fan, X., Fu, Y., Goloub, P., Jiang, H., Liu, Q., Mai, B., Wang, P., Wu, Y., Zhang, J., Zhang, R., and Zhang, X.: Ground-based remote sensing of aerosol climatology in China: Aerosol optical properties, direct radiative effect and its parameterization, Atmos. Environ., 124, Part B, 243-251, 2016, https://doi.org/10.1016/j.atmosenv.2015.05.071.

Xie, Y., Zhang, Y., Xiong, X.X, Qu, J.J., and Che, H.Z.: Validation of MODIS aerosol optical depth product over China using CARSNET measurements, Atmos. Environ., 45, 5970-5978, 2011.

Xin, J., Wang, Y., Li, Z., Wang, P., Hao, W., Nordgren, B., Wang, S., Liu, G., Wang, L., Wen, T., Sun, Y., and Hu, B.: Aerosoloptical depth (AOD) and angstrom exponent of aerosols observed by the Chinese Sun Hazemeter Networkfrom August 2004 to September 2005, J. Geophys. Res., 112 (D05203), 2007.

Xin, J.Y., Zhang, Q., Gong, C.S., Wang, Y.S., Du, W.P., and Zhao, Y.F.: Aerosol direct radiative forcing over Shandong Peninsula in East Asia from 2004 to 2011, Atmos. Ocean. Sci. Lett., 7, 74-79, 2014.

Xu, X., and Wang, J.: Retrieval of aerosol microphysical properties from AERONET photopolarimetric measurements: 1. Information content analysis, J. Geophys. Res. Atmos., 120, 7059–7078, doi:10.1002/2015JD023108, 2015.

Xu, X., Wang, J., Zeng, J., Spurr, R., Liu, X., Dubovik, D., Li L., Li, Z., Mishchenko, M.I., Siniuk, A., and Holben B.N.: Retrieval of aerosol microphysical properties from AERONET photopolarimetric measurements: 2. A new research algorithm and case demonstration, J. Geophys. Res. Atmos., 120, 7079–7098, doi:10.1002/2015JD023113, 2015.

925 Yang, M., Howell, S.G., Zhuang, J., and Huebert, B.J.: Attribution of aerosol light absorption to
926 black carbon, brown carbon, and dust in China – interpretations of atmospheric measurements
927 during EAST-AIRE, Atmos. Chem. Phys., 9, 2035–2050,
928 http://www.atmos-chem-phys.net/9/2035/2009/, doi:10.5194/acp-9-2035-2009, 2009.
929 Zhang, L., Sun, J. Y., Shen, X. J., Zhang, Y. M., Che, H., Ma, Q. L., Zhang, Y. W., Zhang, X. Y.,
930 and Ogren, J. A.: Observations of relative humidity effects on aerosol light scattering in the
931 Yangtze River Delta of China, Atmos. Chem. Phys., 15, 8439-8454,
932 doi:10.5194/acp-15-8439-2015, 2015.
933 Zhang, Q., Streets, D., Carmichael, G., He, K., Huo, H., Kannari, A., Klimont, Z., Park, I.S.,
934 Reddy, S., Fu, J., Chen, D., Duan, L., Lei, Y., Wang, L., and Yao, Z.L.: Asian emissions in 2006
935 for the NASA INTEX-B mission, Atmos. Chem. Phys., 9,5131-5153,
936 doi:10.5194/acp-9-5131-2009, 2009.
937 Zhang, X., Wang, Y., Niu, T., Zhang, X., Gong, S., Zhang, Y., and Sun, J.: Atmospheric aerosol
938 compositions in China: spatial/temporal variability, chemical signature, regional haze
939 distribution and comparisons with global aerosols. Atmos. Chem. Phys., 12, 779–799,
940 http://dx.doi.org/10.5194/acp-12-779-2012, 2012.
941 Zhao, H., Che, H., Zhang, X., Ma, Y., Wang, Y., Wang, X., Liu, C., Hou, B., and Che, H.:
942 Aerosol optical properties over urban and industrial region of Northeast China by using
943 ground-based sun-photometer measurement, Atmos. Environ., 75, 270–278, 2013.
944 Zhao, H., Che, H., Ma, Y., Xia, X., Wang, Y., Wang, P, and Wu, X.: Temporal variability of the
945 visibility, particulate matter mass concentration and aerosol optical properties over an urban
946 site in Northeast China. Atmos. Res., 166, 204-212, 2015.
947 Zheng, C., Zhao, C., Zhu, Y., Wang, Y., Shi, X., Wu, X., Chen, T., Wu, F., and Qiu, Y.: Analysis
948 of Influential Factors for the Relationship between PM2.5 and AOD in Beijing, Atmos. Chem.
949 Phys. Discuss., https://doi.org/10.5194/acp-2016-1170, in review, 2017.
950 Zhu, J., Che, H., Xia, X., Chen, H.B, Goloub, P., and Zhang, W.: Column-integrated aerosol
951 optical and physical properties at a regional background atmosphere in North China Plain,
952 Atmos. Environ., 84,54–64, 2014.
953 Zhuang, B., Wang, T., Li, S., Liu, J., Talbot, R., Mao, H., Yang, X., Fu, C., Yin, C., Zhu, J., Che,
954 H., and Zhang, X.: Optical properties and radiative forcing of urban aerosols in Nanjing over
955 China, Atmos. Environ., 83, 43–52, 2014.
956 Zhuang, B., Wang, T., Liu, J., Che, H., Han, Y., Fu, Y., Li, S., Xie, M., Li, M., Chen, P., Chen, H.,
957 Y, X., and Sun, J.: The optical, physical properties and direct radiative forcing of urban

958 columnar aerosols in Yangtze River Delta, China, Atmos. Chem. Phys. Discuss.,
959 https://doi.org/10.5194/acp-2017-215, 2017.

960 Figure captions

961 Figure 1. Locations and elevations of the seven CARSNET sites in the Yangtze River Delta.

962 Figure 2.Temporal variations in the aerosol volume-size distributions at (a) Hangzhou, (b)
963 Xiaoshan, (c) Fuyang, (d) LinAn, (e) Tonglu, (f) Jiande and (g) ChunAn.

964 Figure 3. Variations in the total, fine- and coarse-mode $AOD_{440\ nm}$ at (a) Hangzhou, (b)
965 Xiaoshan, (c) Fuyang, (d) LinAn, (e) Tonglu, (f) Jiande and (g) ChunAn. The boxes represent
966 the 25th to 75th percentiles of the distributions while the dots and solid lines within each box
967 represent the means and medians, respectively.

968 Figure 4. Variations in the single scattering albedo at 440, 670, 870, and 1020 nm at (a)
969 Hangzhou, (b) Xiaoshan, (c) Fuyang, (d) LinAn, (e) Tonglu, (f) Jiande and (g) ChunAn. See
970 Figure 3 for an explanation of the symbols.

971 Figure 5. (a) Annual average absorption aerosol optical depths at 440 nm ($AAOD_{440\ nm}$) at the
972 CARSNET sites and month-to-month variations in $AAOD_{440\ nm}$ at (b) Hangzhou, (c) Xiaoshan,
973 (d) Fuyang, (e) LinAn, (f) Tonglu, (g) Jiande and (h) ChunAn. See Figure 3 for an explanation
974 of the symbols.

975 Figure 6. (a) Annual variations of monthly mean direct aerosol radiative forcing (50-80 degrees
976 SZA) at the bottom of the atmosphere over (b) Hangzhou, (c) Xiaoshan, (d) Fuyang, (e) LinAn,
977 (f) Tonglu, (g) Jiande and (h) ChunAn. See Figure 3 for an explanation of the symbols.

978 Figure 7. (a) Annual variations in the monthly mean direct aerosol radiative forcing (50-80
979 degrees SZA) at the top of the atmosphere (TOA) at (b) Hangzhou, (c) Xiaoshan, (d) Fuyang,
980 (e) LinAn, (f) Tonglu, (g) Jiande and (h) ChunAn. See Figure 3 for an explanation of the
981 symbols.

982 Figure 8. The aerosol type classification using SSA as a function of $AE_{440–870\ nm}$ over (a)
983 Hangzhou, (b) Xiaoshan, (c) Fuyang, (d), LinAn, (e) Tonglu, (f) Jiande and (g) ChunAn. See
984 text for description of groups I–VII.

985 Figure 9. The distribution of the aerosol type classification over (a) Hangzhou, (b) Xiaoshan, (c)
986 Fuyang, (d), LinAn, (e) Tonglu, (f) Jiande and (g) ChunAn. See text for description of types I–
987 VII.

988 Figure 1. Locations and elevations of the seven CARSNET sites in the Yangtze River Delta.

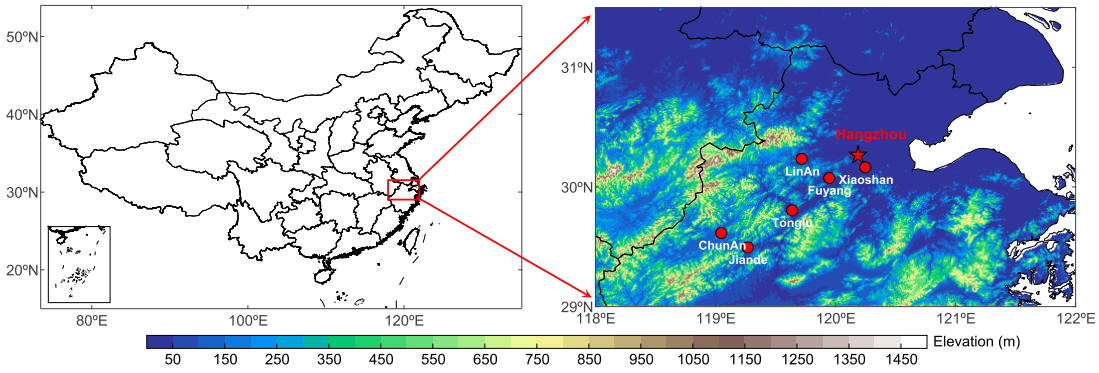

989

990

991 Figure 2.Temporal variations in the aerosol volume-size distributions at (a) Hangzhou, (b)

992 Xiaoshan, (c) Fuyang, (d) LinAn, (e) Tonglu, (f) Jiande and (g) ChunAn.

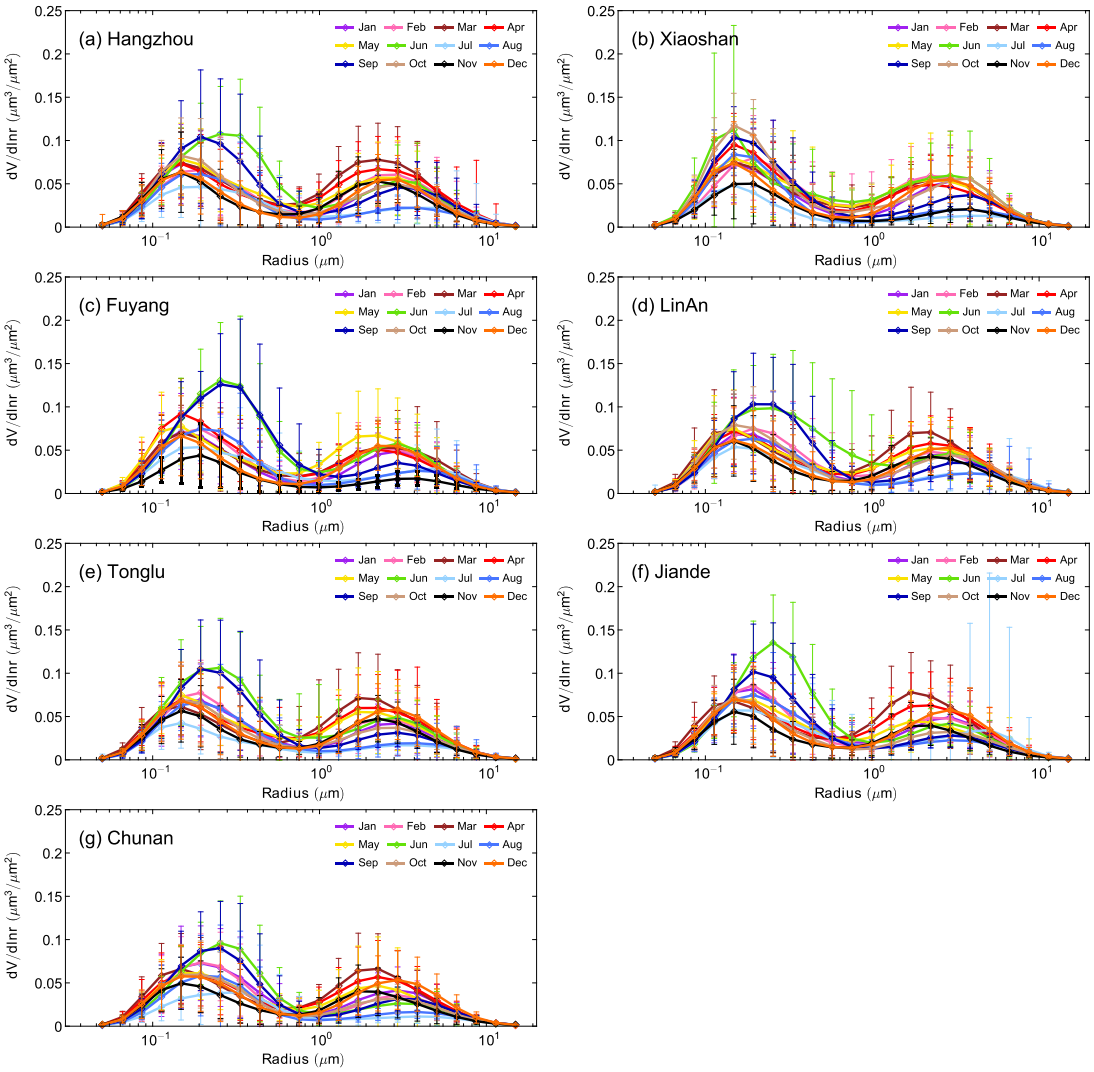

993

994

995

Figure 3. Variations in the total, fine- and coarse-mode $AOD_{440\ nm}$ at (a) Hangzhou, (b) Xiaoshan, (c) Fuyang, (d) LinAn, (e) Tonglu, (f) Jiande and (g) ChunAn. The boxes represent the 25th to 75th percentiles of the distributions while the dots and solid lines within each box represent the means and medians, respectively.

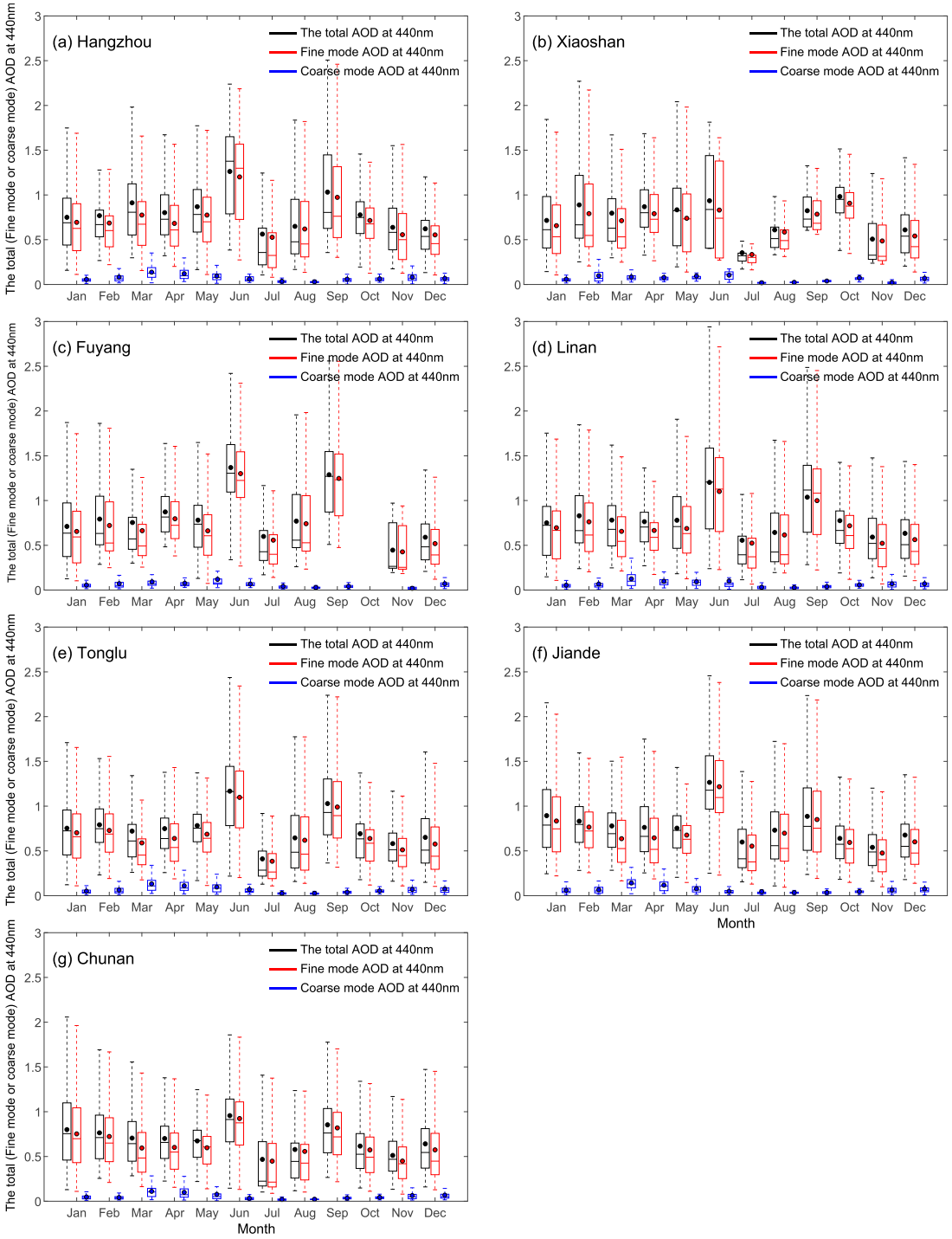

Figure 4. Variations in the single scattering albedo at 440, 670, 870, and 1020 nm at (a) Hangzhou, (b) Xiaoshan, (c) Fuyang, (d) LinAn, (e) Tonglu, (f) Jiande and (g) ChunAn. See Figure 3 for an explanation of the symbols.

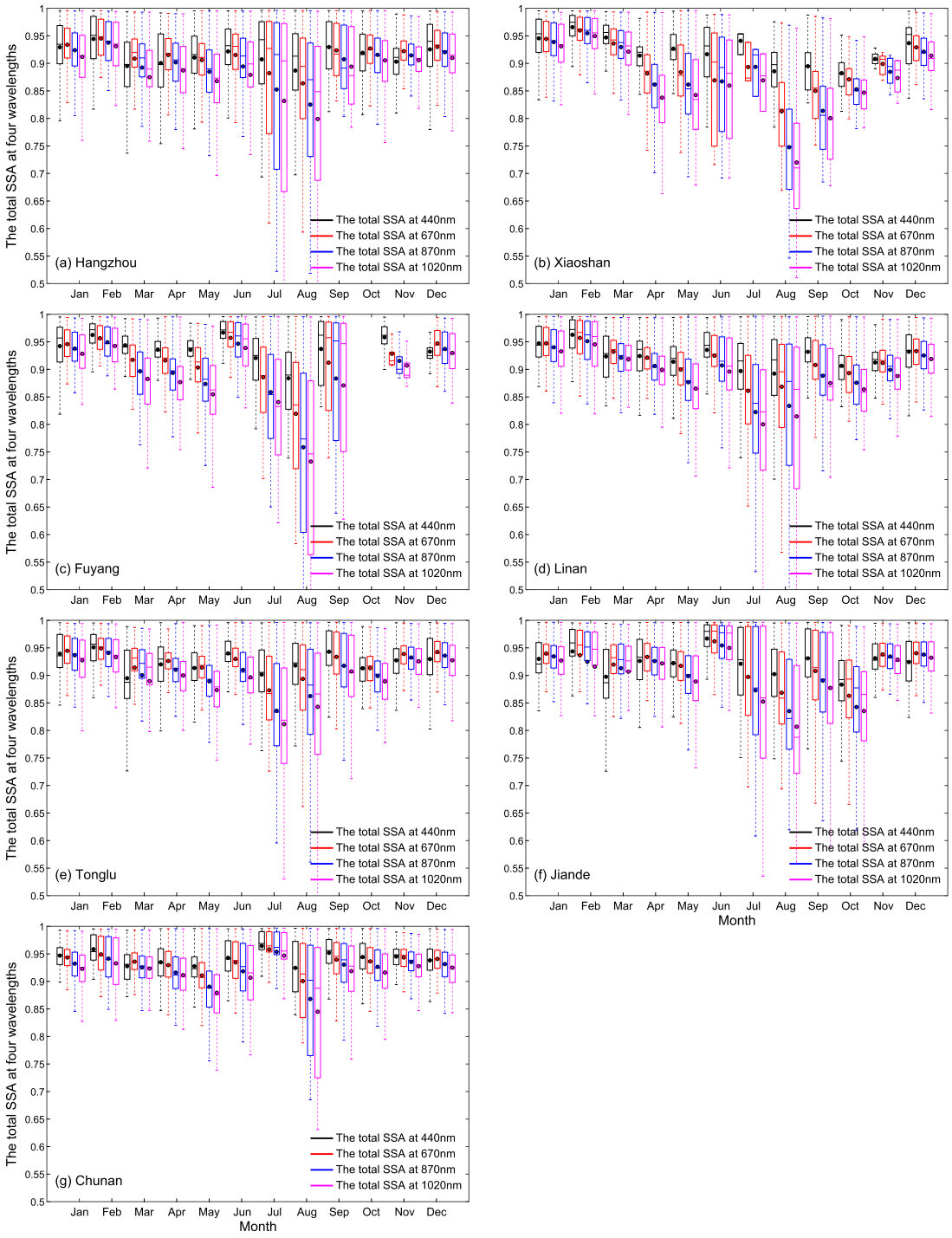

1007 Figure 5. (a) Annual average absorption aerosol optical depths at 440 nm ($AAOD_{440\ nm}$) at the
1008 CARSNET sites and month-to-month variations in $AAOD_{440\ nm}$ at (b) Hangzhou, (c) Xiaoshan,
1009 (d) Fuyang, (e) LinAn, (f) Tonglu, (g) Jiande and (h) ChunAn. See Figure 3 for an explanation
1010 of the symbols.

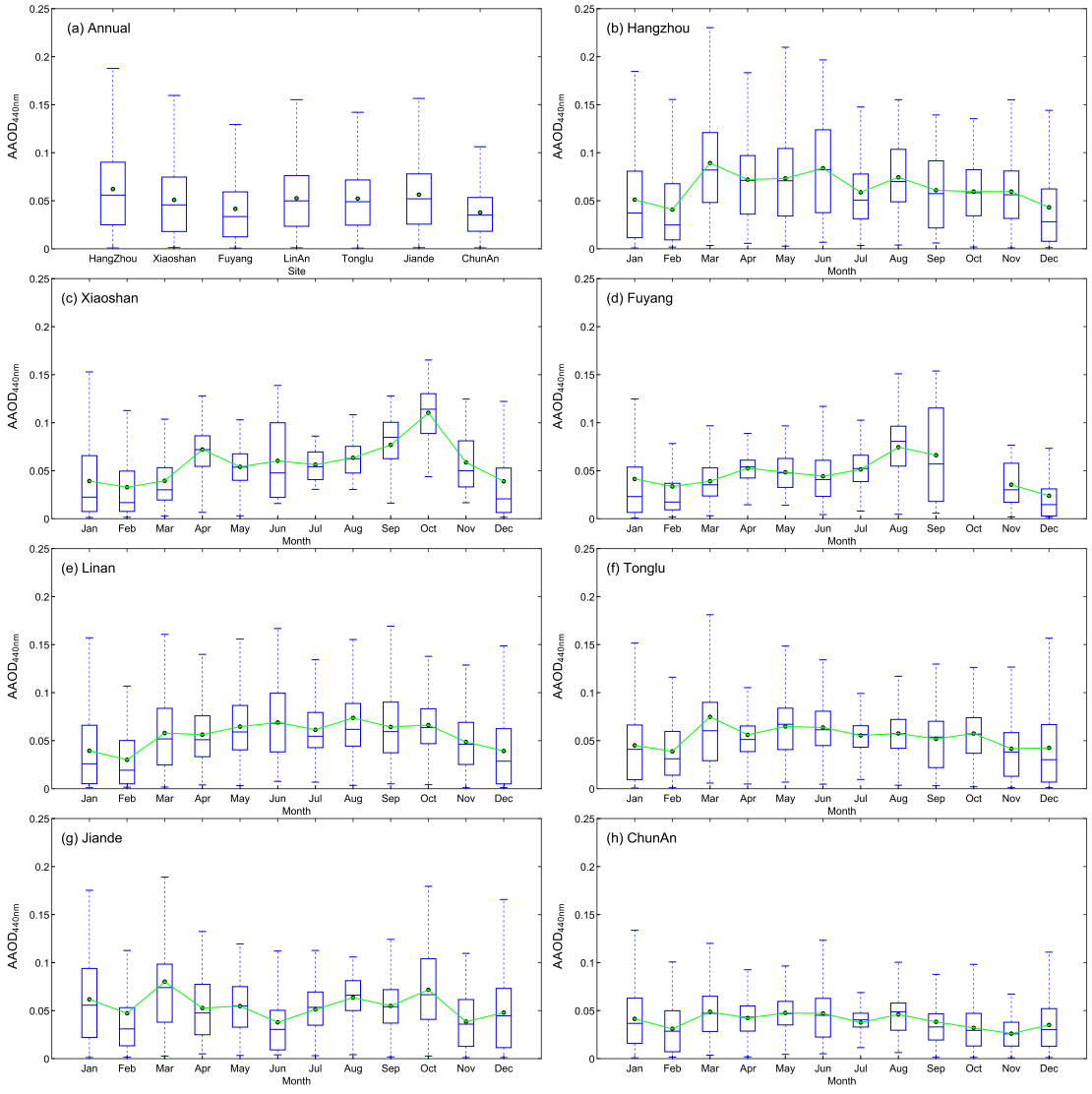

1011

1012

Figure 6. (a) Annual variations of monthly mean direct aerosol radiative forcing (50-80 degrees SZA) at the bottom of the atmosphere over (b) Hangzhou, (c) Xiaoshan, (d) Fuyang, (e) LinAn, (f) Tonglu, (g) Jiande and (h) ChunAn. See Figure 3 for an explanation of the symbols.

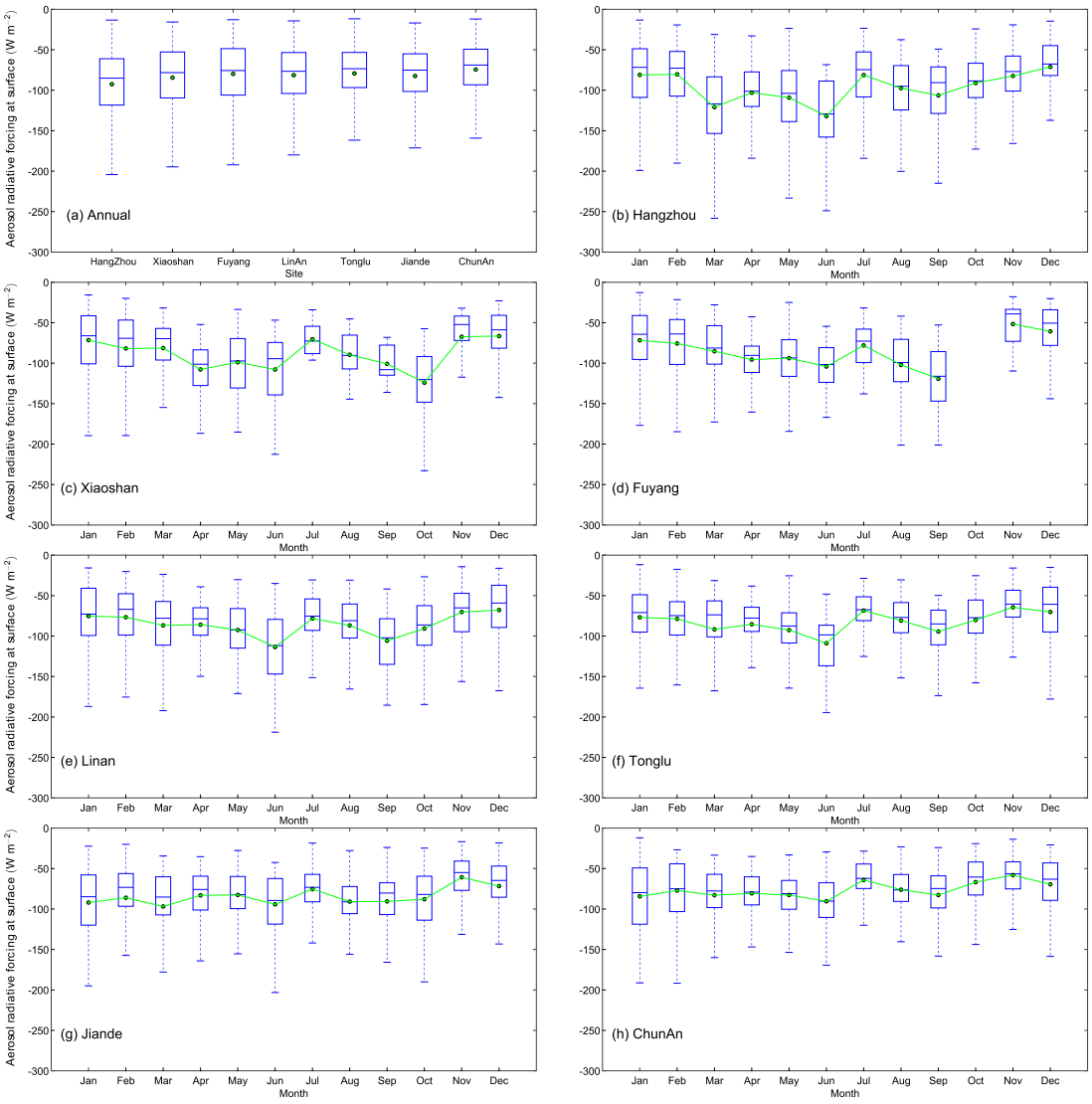

Figure 7. (a) Annual variations in the monthly mean direct aerosol radiative forcing (50-80 degrees SZA) at the top of the atmosphere (TOA) at (b) Hangzhou, (c) Xiaoshan, (d) Fuyang, (e) LinAn, (f) Tonglu, (g) Jiande and (h) ChunAn. See Figure 3 for an explanation of the symbols.

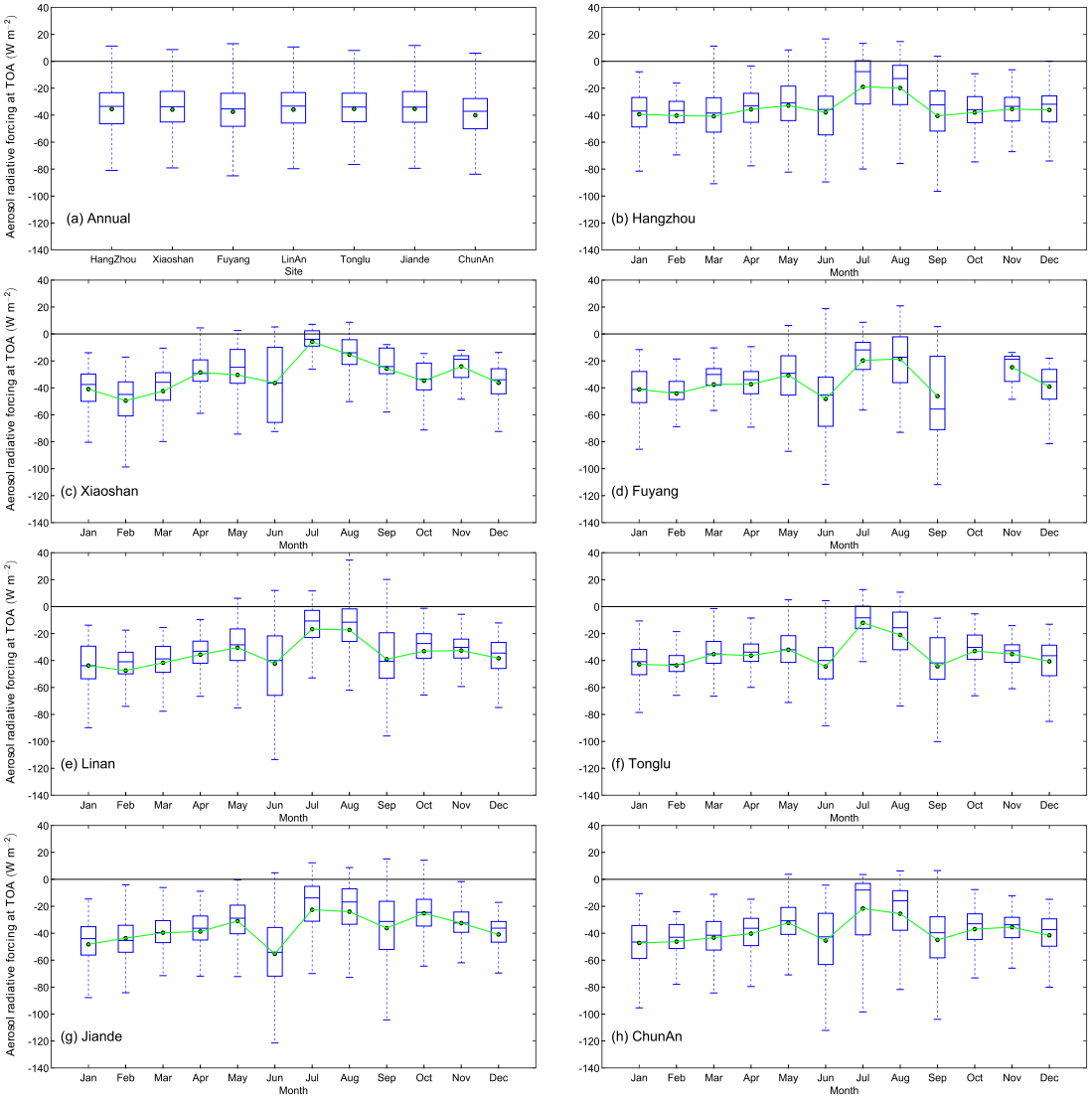

Figure 8. The aerosol type classification using SSA as a function of $AE_{440–870\ nm}$ over (a) Hangzhou, (b) Xiaoshan, (c) Fuyang, (d), LinAn, (e) Tonglu, (f) Jiande and (g) ChunAn. See text for description of groups I–VII.

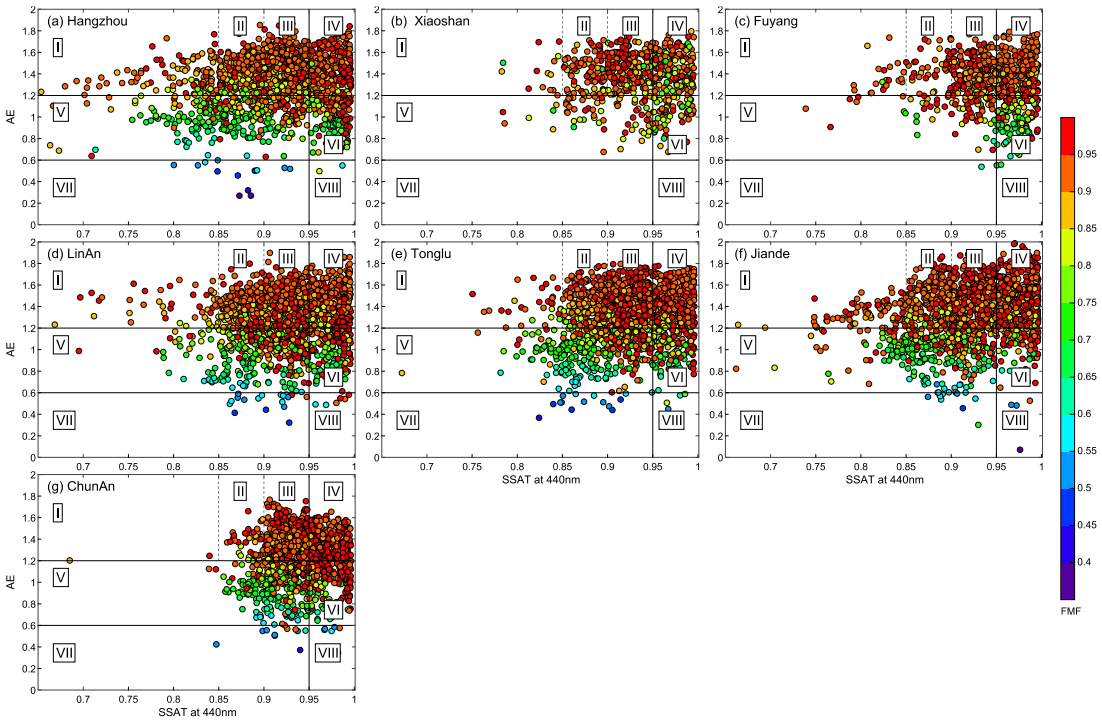

Figure 9. The distribution of the aerosol type classification over (a) Hangzhou, (b) Xiaoshan, (c) Fuyang, (d), LinAn, (e) Tonglu, (f) Jiande and (g) ChunAn. See text for description of types I–VII.

(a) Hangzhou

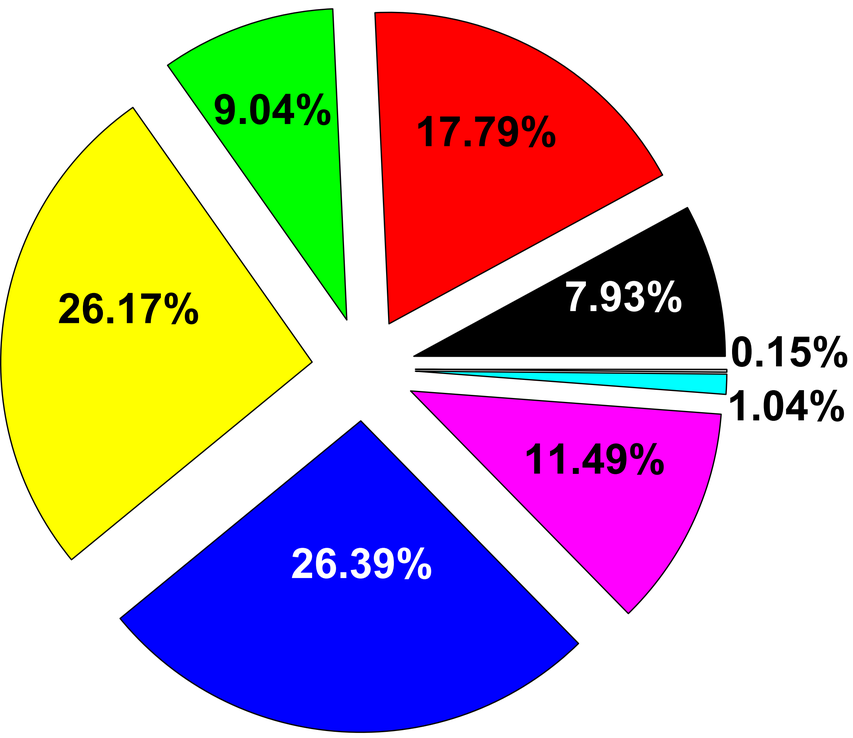

(b) Xiaoshan

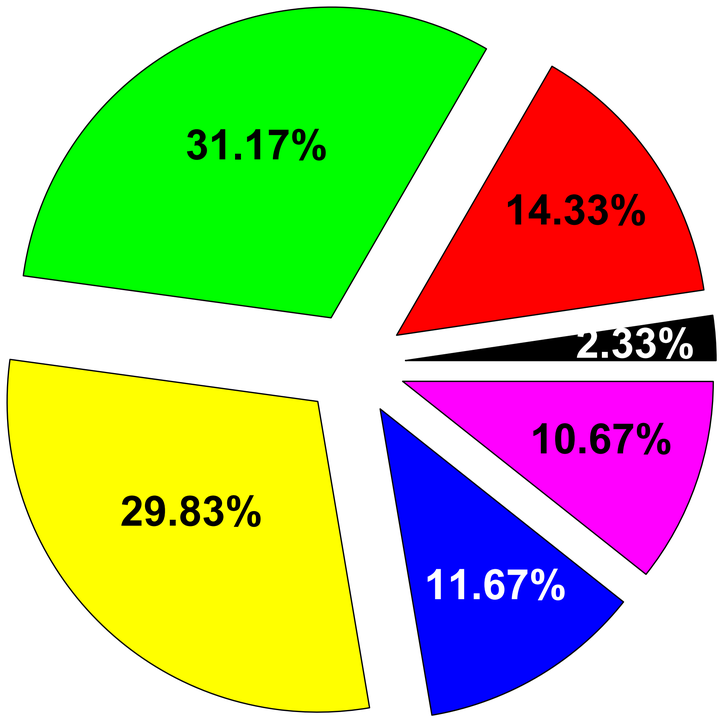

(c) Fuyang

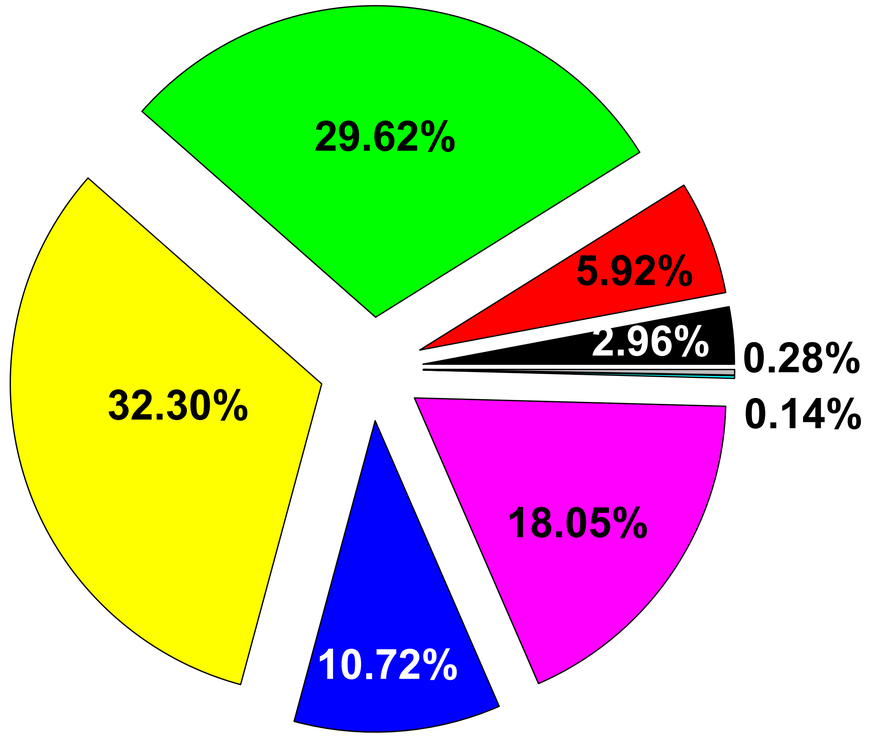

(d) LinAn

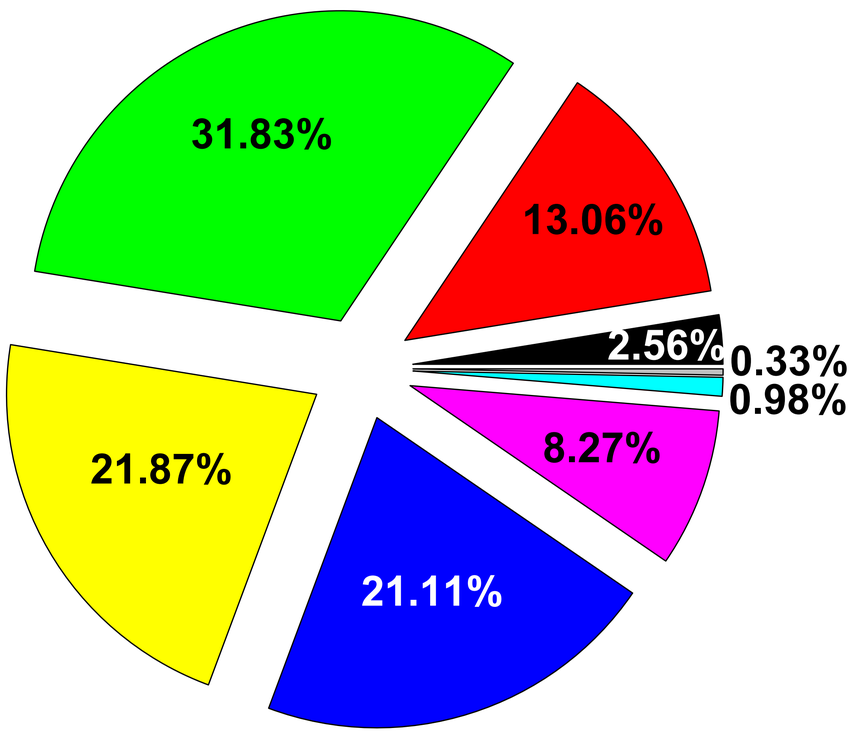

(e) Tonglu

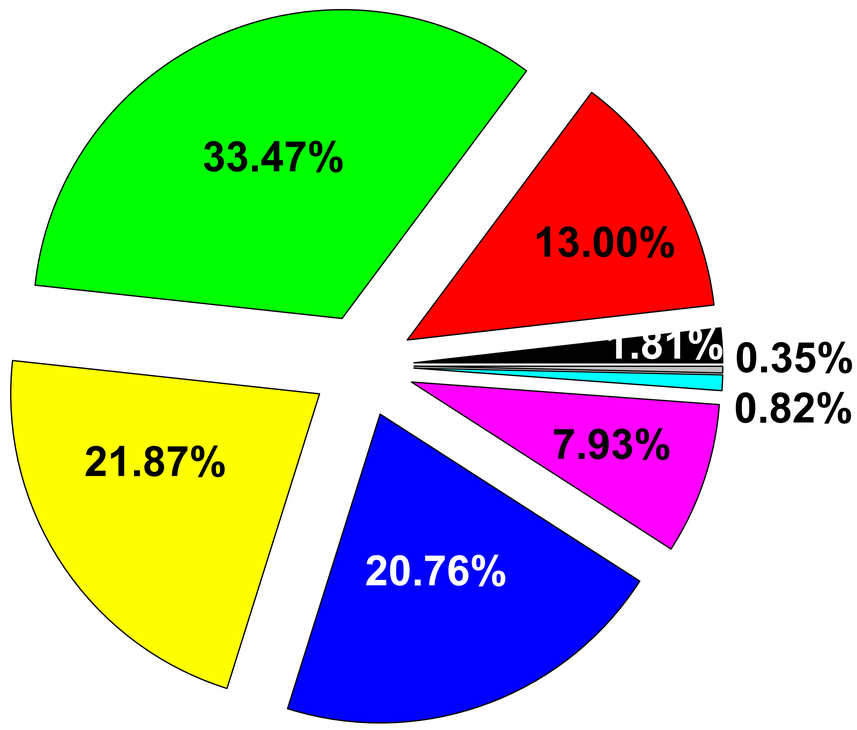

(f) Jiande

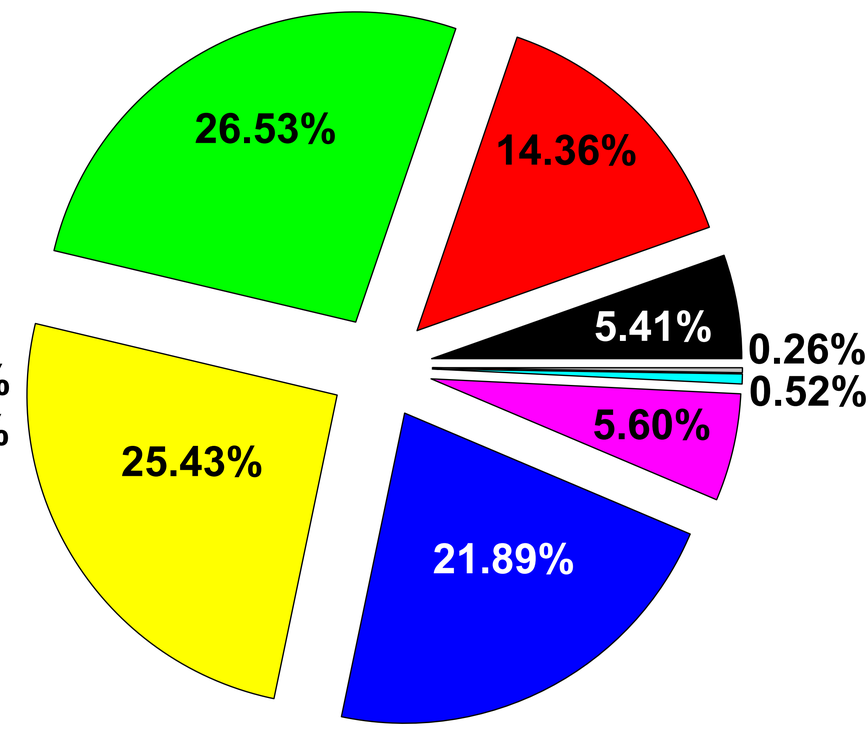

(g) ChunAn

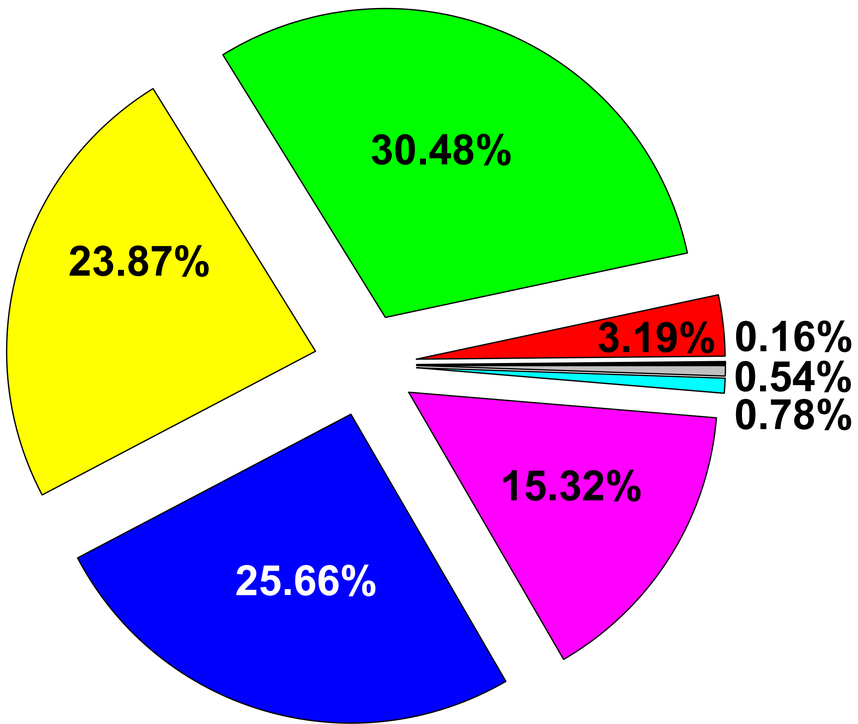

Type I
Type II
Type III
Type IV
Type V
Type VI
Type VII
Type VIII

1033 Supplement

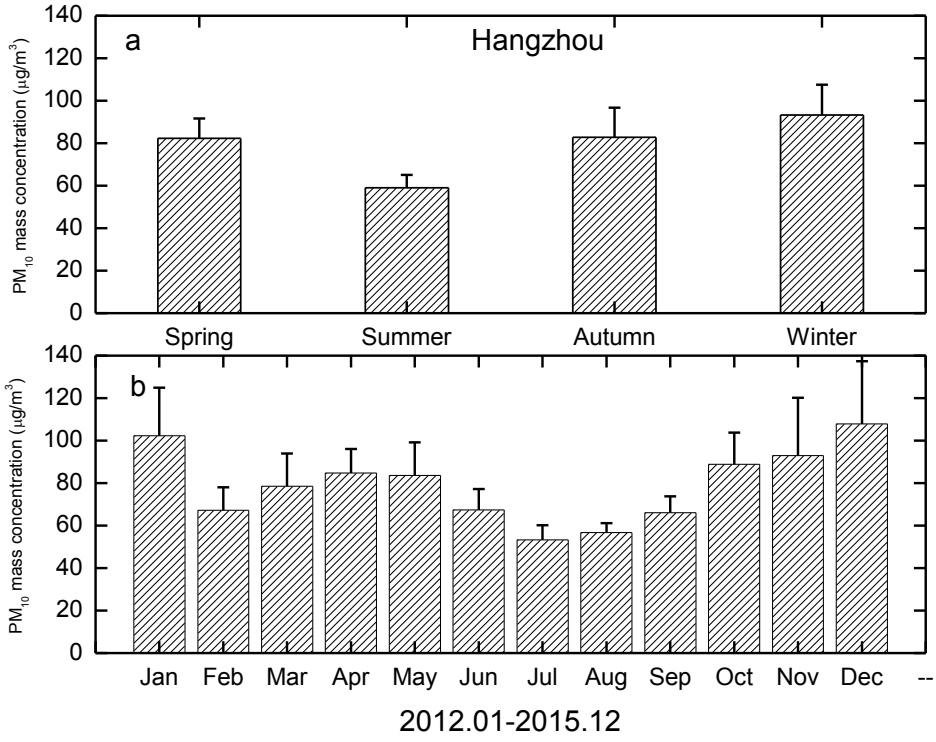

1034

1035 Seasonal and monthly variations of PM10 mass concentrations (μg/m^3) in Hangzhou

1036 during 2012-2015

1037

1038